Pergamon

Int. J. Solids Structures Vol. 35, Nos 28–29, pp. 3755–3791, 1998

0020-7683/98 $19.00 + .00

PII: S0020-7683(97)00177-7

NUMERICAL SIMULATIONS OF DYNAMIC PLASTIC SHEAR INSTABILITY UNDER CONDITIONS OF PLANE STRAIN

YOUNGSEOG LEE and VIKAS PRAKASH*
Department of Mechanical and Aerospace Engineering, Case Western Reserve University, Cleveland, OH 044106, U.S.A.

(*Received* 9 *March* 1997; *in revised form* 10 *June* 1997)

Abstract—The present paper presents a numerical analysis for the edgewise propagation of plastic instability from the tip of a pre-existing semi-infinite notch in an otherwise unbounded continuum. The driving force for the shear deformation is provided by an in-plane shear loading pulse. Coupled thermo-mechanical simulations are carried out under fully plane strain conditions. The simulations take into account finite deformations, inertia, heat conduction, thermal softening, strain hardening and strain rate hardening. A combined power law-exponential relation that gives rise to enhanced strain-rate hardening and ultra-high strain rates is employed. In order to investigate the effects of material parameters on the initiation and progression of plastic instability, a series of numerical simulations are conducted by varying the material model parameters that govern material strain hardening, strain rate sensitivity and thermal softening. Additionally, simulations assuming fully adiabatic conditions and those incorporating heat conduction are carried out separately.

The results of the simulations confirm the existence of an active plastic zone ahead of the propagating plastic shear instability. In the active plastic zone the gradients in flow stress, the plastic strains, the plastic strain rates and temperature are relatively small in the direction along the propagation of the shear instability as compared to the direction normal to it. The region behind the propagating instability exhibits highly localized shear deformation and intense heating. The intense heating results in thermal softening and hence a decrease in the flow stress in this localized region. Also, in the localized region just ahead of the notch tip, the equivalent plastic strain rate after an initial increase is observed to decrease with the applied shearing deformation. The decrease in both the flow stress and the equivalent plastic strain rate leads to a non-zero monotonically decreasing dissipation in the vicinity of the notch tip. Moreover, the plastic dissipation reaches a maximum just behind the tip of the propagating shear instability. Moreover, the results of these simulations indicate that the initiation and progression of the plastic instability are significantly affected by changes in the strain hardening parameter and the strain rate sensitivity of the material. Enhanced strain rate sensitivity is observed to drastically retard the initiation and the progression of plastic instability, whereas the reduced strain hardening results in a considerable decrease in the time required for the initiation of plastic instability and consequently an increase in the overall growth of the plastic instability.

In an attempt to characterize the energy absorbed by the material during the development of the plastic shearing instability, J-integral values are calculated for the various material models employed in the present study. It is observed that the J-integral is the highest for the material showing the smallest progression of the plastic instability (material model with enhanced strain rate sensitivity), and lowest for the material showing the largest extension of plastic instability (material model with reduced strain hardening coefficient). These observations reiterate the concept of shear band toughness introduced by Grady (1992). © 1998 Elsevier Science Ltd. All rights reserved.

1. INTRODUCTION

Plastic shear instability is a strain localization phenomenon that occurs most frequently during dynamic plastic deformation of a significant number of commercial purity metals, their alloys and polymers. Such instabilities are precursors to adiabatic shear bands, and can lead to initiation and propagation of failure. Even for cases in which the localization of plastic instability does not lead to fracture, the understanding of the formation of these bands is still important since localized plastic deformation can greatly influence the subsequent plastic deformation. Thus, in view of their significance as a precursor to fracture and as a mechanism of large plastic deformation, the study of localized plastic deformation has found a diverse series of applications including ultra-high speed machining, high velocity shaping and forming operations, crash-worthiness of vehicles, and in the development of a

* Author to whom correspondence should be addressed.

variety of armor and anti-armor concepts. Comprehensive reviews of work in this area have been presented by Argon (1973), Bedford *et al.* (1974), Rogers (1979, 1983), Clifton (1980), Olson *et al.* (1981), Hutchinson (1984), Timothy (1987), and Meyers (1994).

Most of the experimental, analytical and numerical studies carried out in the past to investigate the localization of shearing deformation have focused on understanding the stability of homogeneous deformations to perturbations in either temperature, stress or strain in homogeneous isotropic solids (Recht, 1964; Culver, 1973; Staker, 1981; Bai, 1981; Merzer, 1982; Wright, 1987; Duffy and Chi, 1992; Needleman, 1989; Nemat-Nasseer, 1992 and Zurek, 1994). The general consensus emerging from these studies is that the primary mechanism for localization is a thermo-mechanical one, through which the plastic instability is determined by the net interaction of softening and hardening features of the material behavior. High nominal strain-rates give rise to favorable conditions for the localization of adiabatic deformation by allowing non-uniform heating and non-uniform straining to occur. Whether or not these mechanisms are sufficient in the development of the plastic instability also depends upon the strain-rate sensitivity, heat conduction, inertia, the strength of the initial homogeneities and the imposed boundary conditions.

Unfortunately, the assumptions under which most of the aforementioned plastic localization studies have been carried out do not depict the formation of these bands with sufficient realism. In these studies the localized bands are considered as an one-dimensional entity with their initiation and growth assumed to occur instantaneously over an entire planar cross-section. In reality, these bands originate within a localized region and have well defined fronts which propagate with finite speeds along the plane of shear deformation much like propagating Mode-II cracks (Marchand and Duffy, 1988; Meyers, 1994). Thus, the multi-dimensional nature of these problems assigns them attributes that are normally not present in one-dimensional plastic instability localization models. These characteristics include a dynamically propagating tip, and thus a strong dependence of thermal and mechanical fields on the speed of propagation.

Previous analyses of shear band localization from pre-existing geometric inhomogeneities has been carried out by Marchand and Duffy (1988) in several metal alloys, Kuriyama and Meyers (1986) in HY-TUF steel, Kalthoff and Winkler (1987) in high strength maraging steels, Ravi-Chandar (1995) in polycarbonate, Mason *et al.* (1994) and Zhou *et al.* (1996a, b) in C-300 steel and Ti-6Al-4V alloy. Marchand and Duffy (1988) observed the non-uniform initiation and propagation of shear bands in thin-walled tubular specimens subjected to dynamic torsional loading. They reported an estimated shear band tip speed of 500 m/s. Kuriyama and Meyers (1986), employing an adiabatic constitutive relations for material response, investigated the critical conditions existing at the shear band tip for the onset and propagation of the shear localization. However, their highly simplified numerical analysis neglected the effects of inertia, thermal conductivity and the strain rate sensitivity of the material, all of which are known to have a profound effect on the initiation and propagation of shear bands in a material. Kalthoff and Winkler (1987), using the experimental method of caustics, developed an experimental technique for subjecting edge cracks in plate specimens to high rates of shear loading (near Mode II conditions). In their experiments on high strength maraging steels they observed that at low impact velocities the failure involved shear localization leading to ductile fracture whereas at higher impact velocities failure occurs by ductile fracture. The same fracture mode transition was observed by Ravi-Chandar (1995) in polycarbonate using a loading arrangement similar to that employed by Kalthoff and Winkler (1987), but with a single edge-cracked specimen. Employing a similar specimen and loading configuration, Mason *et al.* (1994) used the method of coherent gradient sensing (CGS) to record the deformation fields around a propagating adiabatic shear band emanating from a pre-machined notch in C-300 steel. They observed that during the early times after impact, the resulting fringe pattern surrounding the shear band resembles the deformation characteristics of a mode II Dugdale plastic zone under small-scale yielding conditions. Also, using a similar experimental geometry, Zhou *et al.* (1996a) measured the real-time temperature history along and perpendicular to the shear band path in C-300 steel specimens by means of high speed infrared detector system. They reported temperatures as high as 1400°C (90% of the melting

point of C-300 steel) and shear band speeds of approximately 1200 m/s (40% of the shear wave speed in C-300). Recently, Grady (1992, 1994) has presented a numerical analysis focusing on energy dissipation during dynamic adiabatic shear banding process. The analysis sheds light on the properties of the shear band process zone including its width and length and the shear displacement accumulated within this region. The energy dissipated within the shear band process zone is also obtained from their model and the concept of shear band toughness is introduced. Wright and Walters (1994) have presented a simple mathematical model for examining the edgewise propagation of a shear band occupying a half-plane of material. Using a rigid-plastic material model with linear thermal softening and power-law rate hardening but without work-hardening they obtained a two parameter solution for the mechanical and thermal fields near the tip of a propagating antiplane shear band.

In the present study, a finite element approach is employed to examine the initiation and edgewise propagation of plastic instability in 4340 VAR steel from the tip of a pre-existing semi-infinite notch in an otherwise unbounded continuum. The driving force for the shear deformation at the notch tip is provided by an in-plane shear loading pulse. The objective of the study is to, (a) examine the deformation and thermal fields during the initiation and propagation of plastic instability from a crack tip under fully plane strain loading conditions, and, (b) understand the role of the various material parameters such as strain hardening coefficient, strain rate sensitivity, thermal softening and thermal conductivity on the initiation and propagation of the plastic instability. The particular boundary problem analyzed is similar to the one used by Ravichandran and Clifton (1989), Prakash and Clifton (1992), and Lee and Prakash (1995) to investigate the plane-strain dynamic fracture under plane wave tensile loading, with the exception that an in-plane shear pulse is employed instead of the normal tensile pulse. The finite element formulation employed takes full account of the effects of finite geometry changes, the material inertia, the effect of the material strain hardening, strain-rate sensitivity and thermal softening. The material is characterized as an isotropically hardening elastic–viscoplastic von Mises solid. In order to investigate the effects of material parameters on the initiation and progression of plastic instability numerical studies are conducted by varying the strain hardening, the strain rate, the strain rate sensitivity and the thermal softening parameters. Moreover, a combined power-law and exponential plastic strain-rate relation, that gives rise to enhanced strain-rate hardening at ultra-high strain rates, is employed (Clifton, 1990). To investigate the effects of heat conduction on the initiation and propagation of the plastic instability, finite element simulations assuming fully adiabatic conditions and those incorporating heat conduction are carried out separately. The study of the thermal process is important since adiabatic shear banding is primarily driven by thermal softening due to heat generated by plastic flow.

2. PROBLEM FORMULATION

The analysis is based on a convected Lagrangian formulation of field equations with the initial undeformed body configuration as the reference. Convected coordinates y^i are introduced which serve as particle labels. Relative to a fixed Cartesian frame, the position of a material point in the reference configuration is given by $\mathbf{X}(y^i)$. The corresponding material particle in the current configuration is located by a position vector $\mathbf{x}(y^i)$. The base vectors for the reference and the current configuration of the body are denoted by $\mathbf{g}_i$ and $\bar{\mathbf{g}}_i$, respectively, with

$$\mathbf{g}_i = \frac{\partial \mathbf{X}}{\partial y^i} \quad \text{and} \quad \bar{\mathbf{g}}_i = \frac{\partial \mathbf{x}}{\partial y^i}. \tag{1}$$

The reciprocal base vectors can be obtained from their respective base vectors as $\mathbf{g}^i = g^{ij}\mathbf{g}_j$ and $\bar{\mathbf{g}}^i = \bar{g}^{ij}\bar{\mathbf{g}}_j$, where g^{ij} and $\bar{g}^{ij}$ are, respectively, the inverse of the metric tensors $g_{ij} = \mathbf{g}_i \cdot \mathbf{g}_j$ and $\bar{g}_{ij} = \bar{\mathbf{g}}_i \cdot \bar{\mathbf{g}}_j$.

This displacement vector, $\mathbf{u}$, and the deformation gradient tensor $\mathbf{F}$, are defined as

$$\mathbf{u} = \mathbf{x} - \mathbf{X} \quad \text{and} \quad \mathbf{F} = \frac{\partial \mathbf{x}}{\partial \mathbf{X}}. \tag{2}$$

Within the context of the convective coordinate formulation, it follows that the deformed base vectors $\tilde{\mathbf{g}}_i$, are simply the push forward to the reference base vectors $\mathbf{g}_i$, i.e.

$$\tilde{\mathbf{g}}_i = \mathbf{F} \cdot \mathbf{g}_i. \tag{3}$$

A similar result is obtained for the contravariant base vectors

$$\tilde{\mathbf{g}}^i = \mathbf{F}^{-\mathrm{T}} \cdot \mathbf{g}^i. \tag{4}$$

For elastic–plastic deformation, the basic kinematic assumption employed is the multiplicative decomposition of the deformation gradient, Lee (1969)

$$\mathbf{F} = \mathbf{F}^{\mathrm{e}} \cdot \mathbf{F}^{\mathrm{p}}, \tag{5}$$

where $\mathbf{F}^{\mathrm{e}}$ represents the deformation gradient tensor associated with elastic deformation and rigid body rotation, and $\mathbf{F}^{\mathrm{p}}$ is the deformation gradient tensor associated with plastic flow.

The spatial velocity gradient tensor is given by $\mathbf{L} = \dot{\mathbf{F}} \cdot \mathbf{F}^{-1}$. Using the kinematic decomposition, i.e. (5), in the definition of $\mathbf{L}$ yields

$$\mathbf{L} = \mathbf{L}^{\mathrm{e}} + \mathbf{L}^{\mathrm{p}} = \dot{\mathbf{F}}^{\mathrm{e}} \cdot \mathbf{F}^{\mathrm{e}-1} + \mathbf{F}^{\mathrm{e}} \cdot \mathbf{F}^{\mathrm{p}-1} \cdot \dot{\mathbf{F}}^{\mathrm{p}} \cdot \mathbf{F}^{\mathrm{e}-1}, \tag{6}$$

where $(\cdot)$ denotes non-objective material time derivative and $()^{-1}$ denotes tensor inverse.

The rate of deformation and spin tensors are defined as the symmetric and skew-symmetric parts of $\mathbf{L}$, i.e., $\mathbf{D} = \operatorname{sym} \mathbf{L}$ and $\mathbf{W} = \operatorname{skew} \mathbf{L}$. The elastic and plastic parts of $\mathbf{D}$ and $\mathbf{W}$ are identified as

$$\begin{aligned} \mathbf{D}^{\mathrm{e}} + \mathbf{W}^{\mathrm{e}} &= \dot{\mathbf{F}}^{\mathrm{e}} \cdot \mathbf{F}^{\mathrm{e}-1}, \\ \mathbf{D}^{\mathrm{p}} + \mathbf{W}^{\mathrm{p}} &= \mathbf{F}^{\mathrm{e}} \cdot \dot{\mathbf{F}}^{\mathrm{p}} \cdot \mathbf{F}^{p-1} \cdot \mathbf{F}^{\mathrm{e}-1} \end{aligned} \tag{7}$$

where $\mathbf{D}^{\mathrm{e}}$, $\mathbf{D}^{\mathrm{p}}$ and $\mathbf{W}^{\mathrm{e}}$, $\mathbf{W}^{\mathrm{p}}$ are the symmetric and skew-symmetric parts of $\mathbf{L}^{\mathrm{e}}$ and $\mathbf{L}^{\mathrm{p}}$, respectively.

The momentum balance for dynamic deformation of solids, can be written either in the current configuration in terms of the symmetric Cauchy stress tensor, $\boldsymbol{\sigma}$, or in the reference configuration in terms of the symmetric nominal stress tensor (second Piola–Kirchhoff stress), $\tilde{\mathbf{T}}$. These stress measures are related to the force, $\mathbf{df}$, transmitted across a material element by

$$\mathbf{df} = \tilde{\mathbf{n}} \cdot \boldsymbol{\sigma} \, \mathrm{d}\tilde{S} = \mathbf{F} \cdot \mathbf{n} \cdot \tilde{\mathbf{T}} \, \mathrm{d}S. \tag{8}$$

Here, $\mathrm{d}\tilde{S}$ and $\tilde{\mathbf{n}}$ denote the area and orientation of a material element in the current configuration that had a material area $\mathrm{d}S$ and an orientation $\mathbf{n}$ in the reference configuration.

The Kirchhoff stress is defined by $\boldsymbol{\tau} = \det(\mathbf{F})\boldsymbol{\sigma}$. Using Nanson's relation in (8), yields the relationship between the stress measures, $\tilde{\mathbf{T}}$ and $\boldsymbol{\tau}$

$$\tilde{\mathbf{T}} = \mathbf{F}^{-1} \cdot \boldsymbol{\tau} \cdot \mathbf{F}^{-\mathrm{T}}. \tag{9}$$

The dynamic principle of virtual work can be written in the integral form as

$$\int_V \tau^{ij}\delta E_{ij}\,\mathrm{d}V = \int_S f^i \delta u_i\,\mathrm{d}S - \int_V \rho_0 \frac{\partial^2 u^i}{\partial t^2}\delta u_i\,\mathrm{d}V, \tag{10}$$

where V, S, and ρ_0 are the volume, surface area and mass density, respectively, of the body in the reference configuration. In writing (10) we have used the fact that the components of any spatial tensor on the convected (current) base vectors coincide with the components of the pull-back of that tensor on the reference base vectors. Thus, the components of the Kirchhoff stress on the current base vectors coincide with the components of the symmetric nominal stress tensor on the reference base vectors, i.e., $\tilde{\mathbf{g}}^i \cdot \boldsymbol{\tau} \cdot \tilde{\mathbf{g}}^j = \mathbf{g}^i \cdot \tilde{\mathbf{T}} \cdot \mathbf{g}^j$.

The traction vector component f^i on a surface with unit normal vector component n_j in the reference configuration is given by

$$f^i = (\tau^{ij} + \tau^{kj}u^i_{,k})n_j. \tag{11}$$

The Lagrangian strain tensor in the reference configuration is

$$E_{ij} = \tfrac{1}{2}(u_{i,j} + u_{j,i} + u^k_{,i}u_{k,j}), \tag{12}$$

where $(\,)_{,i}$ represents the covariant partial differentiation in the reference frame.

At this point, we will also define quantities $\tilde{\mathbf{T}}^*$ and $\mathbf{E}^e$ which will be useful in the subsequent discussions

$$\tilde{\mathbf{T}}^* = \mathbf{F}^{e-1} \cdot \boldsymbol{\tau} \cdot \mathbf{F}^{e-T}, \quad \mathbf{E}^e = \tfrac{1}{2}(\mathbf{F}^{eT} \cdot \mathbf{F}^e - \mathbf{I}). \tag{13}$$

$\tilde{\mathbf{T}}^*$ and $\mathbf{E}^e$ can be thought of as the stress and elastic strain measures, respectively, on the intermediate configuration.

With body forces and external heat energy source being absent, the balance of energy can be expressed as integrals over the reference configuration

$$\int_V \rho_0 \dot{e}\,\mathrm{d}V + \frac{\mathrm{d}}{\mathrm{d}t}\int_V \frac{1}{2}\rho_0 \dot{\mathbf{u}} \cdot \dot{\mathbf{u}}\,\mathrm{d}V = \int_S \mathbf{f} \cdot \dot{\mathbf{u}}\,\mathrm{d}S - \int_S J\mathbf{n} \cdot \mathbf{F}^{-1} \cdot \tilde{\mathbf{q}}\,\mathrm{d}S, \tag{14}$$

where e is the specific internal energy, $\mathrm{d}/\mathrm{d}t$ is the material time derivative, J is the Jacobian of the deformation, and $\tilde{\mathbf{q}}$ is heat-flux vector normal to the surface in the current configuration.

Then, noting

$$\int_S \mathbf{f} \cdot \dot{\mathbf{u}}\,\mathrm{d}S = \frac{\mathrm{d}}{\mathrm{d}t}\int_V \frac{1}{2}\rho_0 \dot{\mathbf{u}} \cdot \dot{\mathbf{u}}\,\mathrm{d}V + \int_V \boldsymbol{\tau} : \mathbf{D}\,\mathrm{d}V. \tag{15}$$

Equation (14) can be expressed as

$$\int_V \rho_0 \dot{e}\,\mathrm{d}V = \int_V \boldsymbol{\tau} : \mathbf{D}\,\mathrm{d}V - \int_S J\mathbf{n} \cdot \mathbf{F}^{-1} \cdot \tilde{\mathbf{q}}\,\mathrm{d}S. \tag{16}$$

The specific internal energy can be expressed as $e = e(\mathbf{E}^e, \eta\, h_\alpha)$, where η is the specific energy entropy, and h_α are a set of kinematic variables describing the internal arrangement of the material undergoing plastic deformation.

For the problem treated here, it will prove convenient to rewrite the internal energy in terms of the Gibb's free energy, ψ, as

$$e = \psi(\bar{\mathbf{T}}^*, T, h_\alpha) + \eta T + \frac{1}{\rho_0}\bar{\mathbf{T}}^* : \mathbf{E}^e, \tag{17}$$

where T is the absolute temperature.

Using (17) in (16) and rearranging terms, yields

$$\int_V \left[\left(\rho_0 \frac{\partial \psi}{\partial \bar{\mathbf{T}}^*} + \mathbf{E}^e \right) : \dot{\bar{\mathbf{T}}}^* + (\dot{\mathbf{E}}^e : \bar{\mathbf{T}}^* - \tau : \mathbf{D}^e) + \rho_0 \left(\frac{\partial \psi}{\partial T} + \eta \right) \dot{T} + \left(\rho_0 \frac{\partial \psi}{\partial h_\alpha} \dot{h}_\alpha - (1-\chi)\tau : \mathbf{D}^p \right) + \rho_0 T \dot{\eta} \right] \mathrm{d}V = \int_V \chi \tau : \mathbf{D}^p \, \mathrm{d}V - \int_S J\mathbf{n} \cdot \mathbf{F}^{-1} \cdot \bar{\mathbf{q}} \, \mathrm{d}S, \tag{18}$$

where χ represents the fraction of plastic work rate converted to heat and $(1-\chi)$ is the fraction of plastic work rate stored as residual strain energy in the material. In the present analysis χ is taken to have a value of 0.9, which is typical of most metals (Taylor and Quinney, 1934). For all arbitrary values of $\dot{\bar{\mathbf{T}}}^*$ and $\dot{T}$ in (18), we can identify the following relations

$$\begin{aligned} \mathbf{E}^e &= -\rho_0 \frac{\partial \psi}{\partial \bar{\mathbf{T}}^*} \\ \eta &= -\frac{\partial \psi}{\partial T} \\ (1-\chi)\tau : \mathbf{D}^p &= \rho_0 \frac{\partial \psi}{\partial h_\alpha} \dot{h}_\alpha \\ \tau : \mathbf{D}^e &= \dot{\mathbf{E}}^e : \bar{\mathbf{T}}^* \end{aligned} \tag{19}$$

such that (18) reduces to

$$\int_V \rho_0 T \dot{\eta} \, \mathrm{d}V = \int_V \chi \tau : \mathbf{D}^p \, \mathrm{d}V - \int_S J\mathbf{n} \cdot \mathbf{F}^{-1} \cdot \bar{\mathbf{q}} \, \mathrm{d}S. \tag{20}$$

In general, the constitutive relation for heat flux is formulated on the intermediate configuration, i.e.,

$$\bar{\mathbf{q}}^* = -\bar{\mathbf{k}}^* \cdot \mathbf{F}^{eT} \frac{\partial T}{\partial y^i} \bar{\mathbf{g}}^i, \tag{21}$$

where $\bar{\mathbf{q}}^*$ and $\bar{\mathbf{k}}^*$ represent the heat flux vector and thermal conductivity tensor on the intermediate configuration. Formulation of the constitutive relation on the intermediate configuration is necessary to insure that the principle of material frame indifference is not violated. Restricting (21) in cases where thermal conductivity can be assumed to be isotropic, i.e. $\bar{\mathbf{k}}^* = k\mathbf{I}$, the push forward of the heat flux vector in the current configuration yields

$$\bar{\mathbf{q}} = \mathbf{F}^e \cdot \bar{\mathbf{q}}^* = -k \left(\mathbf{F}^e \cdot \mathbf{F}^{eT} \frac{\partial T}{\partial y^i} \bar{\mathbf{g}}^i \right). \tag{22}$$

Restricting attention to cases in which the elastic strains are small in comparison to the plastic strains, $\mathbf{F}^e$ can be approximated as

$$\mathbf{F}^{e} = \mathbf{Q}\cdot(\mathbf{I}+\gamma) \quad \text{where } \mathbf{Q}^{-1} = \mathbf{Q}^{T},$$
$$\gamma = \gamma^{T} \quad \text{and} \quad \|\gamma\| \ll 1. \tag{23}$$

Thus for isotropic constituents with $\|\gamma\| \ll 1$, the heat flux vector in the current configuration becomes

$$\bar{\mathbf{q}} = -k\frac{\partial T}{\partial y^{i}}\bar{\mathbf{g}}^{i}. \tag{24}$$

Substituting (24) in (20) yields the energy balance equation in the reference configuration

$$\int_{V}\rho_0 T\dot{\eta}\,dV = \int_{V}\chi\tau:\mathbf{D}^{p}\,dV + \int_{V}Jk\nabla_0\cdot(\mathbf{F}^{-1}\cdot\mathbf{F}^{-T}\cdot\nabla_0 T)\,dV, \tag{25}$$

where the gradient operator in the reference configuration is denoted by $\nabla_0 = \mathbf{g}^{K}(\partial/\partial y^{K})$.

Using the expression for specific entropy from $(19)_2$ in (25), the balance of energy takes the form

$$-\int_{V}\rho_0 T\frac{\partial^2\psi}{\partial T^2}\dot{T}\,dV - \int_{V}\rho_0 T\frac{\partial^2\psi}{\partial T\partial\bar{\mathbf{T}}^{*}}:\dot{\bar{\mathbf{T}}}^{*}\,dV - \int_{V}\rho_0 T\frac{\partial^2\psi}{\partial T\partial h_{\alpha}}\dot{h}_{\alpha}\,dV = \int_{V}\chi\tau:\mathbf{D}^{p}\,dV + \int_{V}Jk\nabla_0\cdot(\mathbf{F}^{-1}\cdot\mathbf{F}^{-T}\cdot\nabla_0 T)\,dV. \tag{26}$$

The second and third terms on the LHS of (26) represent thermo-elastic coupling with both the recoverable and residual elastic deformation. However, in metals elastic deformation is typically accompanied by only small changes in temperature. In view of this, thermo-elastic coupling is neglected in the present analysis. We also assume that the heat capacity at constant stress, $c_{\bar{\mathbf{T}}^{*}} = -T\partial^2\psi/\partial T^2$, can be approximated by the specific heat at constant pressure c_p. Thus, for the problem considered here, the coupled heat equation takes the simplified form

$$\int_{V}\rho_0 c_p\dot{T}\,dV = \int_{V}\chi\tau:\mathbf{D}^{p}\,dV + \int_{V}Jk\nabla_0\cdot(\mathbf{F}^{-1}\cdot\mathbf{F}^{-T}\cdot\nabla_0 T)\,dV. \tag{27}$$

2.1. *Stress rate–strain rate relations*

Differentiating $(19)_1$ with respect to time yields

$$\dot{\mathbf{E}}^{e} = -\rho_0\frac{\partial^2\psi}{\partial\bar{\mathbf{T}}^{*}\,\partial\bar{\mathbf{T}}^{*}}:\dot{\bar{\mathbf{T}}}^{*} - \rho_0\frac{\partial^2\psi}{\partial T\partial\bar{\mathbf{T}}^{*}}\dot{T} - \rho_0\frac{\partial^2\psi}{\partial T\partial h_{\alpha}}\dot{h}_{\alpha}, \tag{28}$$

or

$$\dot{\mathbf{E}}^{e} = \mathbf{M}:\dot{\bar{\mathbf{T}}}^{*} + \left.\frac{\partial\mathbf{E}^{e}}{\partial\mathbf{T}}\right|_{\bar{\mathbf{T}}^{*},h_{\alpha}}\dot{T} + \left.\frac{\partial\mathbf{E}^{e}}{\partial h_{\alpha}}\right|_{\bar{\mathbf{T}}^{*},T}\dot{h}_{\alpha}, \tag{29}$$

where $\mathbf{M} = -\rho_0\partial^2\psi/\partial\bar{\mathbf{T}}^{*}\,\partial\bar{\mathbf{T}}^{*}$ is the elastic compliance. The third term on the RHS of (29) is neglected for the problem considered here since we assume that the thermo-elastic properties of the material are largely independent of plastic deformation. Furthermore, we can approximate $\partial\mathbf{E}^{e}/\partial T|_{\bar{\mathbf{T}}^{*},h_{\alpha}}$ by a first order expansion about $\bar{\mathbf{T}}^{*} = \mathbf{0}$ such that

$$\left.\frac{\partial \mathbf{E}^e}{\partial T}\right|_{\bar{\mathbf{T}}^*, h_\alpha} = \left.\frac{\partial \mathbf{E}^e}{\partial T}\right|_{\bar{\mathbf{T}}^*=0, h_\alpha} + \frac{\partial \mathbf{M}}{\partial T} : \bar{\mathbf{T}}^* + \text{h.o.t.} \tag{30}$$

The term $\partial \mathbf{E}^e/\partial T|_{\bar{\mathbf{T}}^*=0,h_\alpha}$ represents the thermal expansion tensor, which we will designate as $\boldsymbol{\alpha}$. Neglecting the effects of temperature on the elastic compliance the expression for the elastic strain rate, (29), takes the form

$$\dot{\mathbf{E}}^e = \mathbf{M} : \dot{\bar{\mathbf{T}}}^* + \boldsymbol{\alpha} \dot{T}, \tag{31}$$

(31) can be inverted to yield

$$\dot{\bar{\mathbf{T}}}^* = \mathscr{L} : (\dot{\mathbf{E}}^e - \boldsymbol{\alpha} \dot{T}), \tag{32}$$

where the elastic Moduli are given by $\mathscr{L} = \mathbf{M}^{-1}$.

Using (32), and assuming the existence of a strain energy density function for elastic response, the Jaumann rate of Kirchhoff stress, $\overset{\nabla}{\boldsymbol{\tau}}$, based on the elastic spin rate $\mathbf{W}^e$, can be written as (Needleman, 1985)

$$\overset{\nabla}{\boldsymbol{\tau}} = \dot{\boldsymbol{\tau}} - \mathbf{W}^e \cdot \boldsymbol{\tau} + \boldsymbol{\tau} \cdot \mathbf{W}^e = \mathscr{L}^e : (\mathbf{D}^e - \boldsymbol{\alpha} \dot{T}) + \boldsymbol{\tau} \cdot \mathbf{D}^e + \mathbf{D}^e \cdot \boldsymbol{\tau} \tag{33}$$

where $\dot{\boldsymbol{\tau}}$ is the non-objective material time derivative of the Kirchhoff stress and $\mathscr{L}^e$ is the elastic moduli convected with the elastic deformation gradient, i.e. $\mathscr{L}^e = \mathbf{F}^e \cdot \mathbf{F}^e \cdot \mathscr{L} \cdot \mathbf{F}^{e^T} \cdot \mathbf{F}^{e^T}$. The relation (33) is valid for finite as well as infinitesimal elastic deformations. In applications to metal plasticity, the elastic strains generally remain small as compared to the plastic strains. This implies that the stress magnitude is small compared to the magnitude of any elastic moduli and the last two terms on the RHS of (33) are negligible in comparison with the first term. Moreover constitutive models for plastic spin, $\mathbf{W}^p$, have been considered by several investigators (for example, see Dafalias, 1985). Canova *et al.* (1984) have shown that $\mathbf{W}^p$ is zero for single crystals with very strong rate sensitivity. In view of the lack of well-accepted models for the plastic spin for polycrystaline metals, $\mathbf{W}^p$ is taken to be zero for the analysis used here. For plasticity theories with $\mathbf{W}^p = 0$ the elastic spin rate is identical to the total spin rate. Thus, the elastic Jaumann rate can be replaced by the ordinary Jaumann derivative based on the total material spin $\mathbf{W}$.

The rate of deformation can be expressed as the sum of an elastic part and a part due to plastic straining. Hence, $\mathbf{D} = \mathbf{D}^e + \mathbf{D}^p$. Then, in (33), $\mathbf{D}^e$ can be replaced by $\mathbf{D} - \mathbf{D}^p$ and $\mathbf{W}^e$ by $\mathbf{W}$ (since $\mathbf{W}^p = \mathbf{0}$), which together with the aforementioned approximations yields

$$\overset{\nabla}{\boldsymbol{\tau}} = \dot{\boldsymbol{\tau}} - \mathbf{W} \cdot \boldsymbol{\tau} + \boldsymbol{\tau} \cdot \mathbf{W} = \mathscr{L}^e : (\mathbf{D} - \mathbf{D}^p - \boldsymbol{\alpha} \dot{T}). \tag{34}$$

When the temperature dependence of the elastic moduli is ignored, the tangent moduli for the isotropic elastic response can be written as

$$(\mathscr{L}^e)^{ijkl} = \frac{E}{1+\nu}\left[\frac{1}{2}(\bar{g}^{ik}\bar{g}^{jl} + \bar{g}^{jk}\bar{g}^{il}) + \frac{\nu}{1-2\nu}\bar{g}^{ik}\bar{g}^{jl}\right], \tag{35}$$

where, E is Young's modulus and ν is Poisson's ratio.

For updating the Kirchhoff stresses we need the convected time-derivative of Kirchhoff stresses on the current base vectors. Using an analysis paralleling (Needleman, 1985), the convected derivative of the contravariant components of the Kirchhoff stress can be expressed as

$$\mathring{\boldsymbol{\tau}}^{c} = \mathbf{C} : \mathbf{D} - \mathbf{P}, \tag{36}$$

where $\mathbf{C}$ is a tensor of rank four and $\mathbf{P} = \mathscr{L}^{e} : (\mathbf{D}^{p} + \boldsymbol{\alpha}\dot{T})$. On the current base vectors (36) can be written as

$$(\mathring{\boldsymbol{\tau}}^{c})^{ij} = C^{ijkl}\dot{E}_{kl} - P^{ij}. \tag{37}$$

The Lagrangian strain-rate appears in eqn (37) via the identity $\dot{E}_{ij} = \bar{\mathbf{g}}_i \cdot \mathbf{D} \cdot \bar{\mathbf{g}}_j$, and its components on the reference base vectors are given by

$$\dot{E}_{ij} = \tfrac{1}{2}(F_i^k \dot{F}_{kj} + F_j^k \dot{F}_{ki}). \tag{38}$$

The components of the four tensor $\mathbf{C}$ on the current base vectors can be expressed as

$$C^{ijkl} = (\mathscr{L}^{e})^{ijkl} - \tfrac{1}{2}[\bar{g}^{ik}\tau^{jl} + \bar{g}^{jk}\tau^{il} + \bar{g}^{il}\tau^{jk} + \bar{g}^{jl}\tau^{ik}]. \tag{39}$$

The material is characterized as an isotropically hardening viscoplastic solid for which $\mathbf{D}^{p}$ can be expressed using J_2 flow theory as

$$\mathbf{D}^{p} = \dot{\bar{\varepsilon}}\mathbf{p} \quad \text{where } \mathbf{p} = \frac{3\boldsymbol{\tau}'}{2\bar{\sigma}}. \tag{40}$$

In (40) $\dot{\bar{\varepsilon}}$ is the equivalent plastic strain rate function; the deviatoric stress τ' and the equivalent flow stress $\bar{\sigma}$ are given by

$$\boldsymbol{\tau}' = \boldsymbol{\tau} - \tfrac{1}{3}(\boldsymbol{\tau} : \mathbf{I})\mathbf{I} \quad \text{and} \quad \bar{\sigma}^2 = \tfrac{3}{2}\boldsymbol{\tau}' : \boldsymbol{\tau}'. \tag{41}$$

The material properties used in the present simulations are representative of hardened AISI 4340 VAR steel (200°C temper) (Lee and Prakash, 1996). The plastic strain rate, $\dot{\bar{\varepsilon}}$, is taken to be of the form

$$\dot{\bar{\varepsilon}} = \frac{\dot{\varepsilon}_1 \dot{\varepsilon}_2}{\dot{\varepsilon}_1 + \dot{\varepsilon}_2}, \tag{42}$$

where

$$\dot{\varepsilon}_1 = \dot{\varepsilon}_0 \left[\frac{\bar{\sigma}}{g(\bar{\varepsilon}, T)}\right]^{m}, \quad \dot{\varepsilon}_2 = \dot{\varepsilon}_m \exp\left[-\frac{a g(\bar{\varepsilon}, T)}{\bar{\sigma}}\right] \tag{43}$$

and

$$g(\bar{\varepsilon}, T) = \sigma_0 (1 + \bar{\varepsilon}/\varepsilon_0)^{N} \{1 - \beta[(T/T_0)^{k} - 1]\}. \tag{44}$$

Here, $\bar{\varepsilon} = \int_0^t \dot{\bar{\varepsilon}}\, dt$ is the equivalent plastic strain, $\dot{\varepsilon}_m$ is a reference strain rate, m and a are the rate sensitivity parameters, respectively, σ_0 is a reference stress, ε_0 is a reference strain, N is the strain hardening exponent, T_0 is a reference temperature, and β and k are the thermal softening parameters. The function $g(\bar{\varepsilon}, T)$ represents the stress–strain relation at a quasi-static strain rate of $\dot{\varepsilon}_0$ and at temperature T.

Equation (42), provides a smooth transition between the measured response $\dot{\bar{\varepsilon}} = \dot{\varepsilon}_1(\bar{\sigma}, \bar{\varepsilon}, T)$ at strain rates less than $10^3\ \mathrm{s}^{-1}$, and the limiting behavior $\dot{\bar{\varepsilon}} = \dot{\varepsilon}_2(\bar{\sigma}, \bar{\varepsilon}, T)$ at strain rates greater than, say, $10^5\ \mathrm{s}^{-1}$. The model includes a limiting strain rate $\dot{\varepsilon}_m$ which is not obtainable from experiments; a value of $5 \times 10^8\ \mathrm{s}^{-1}$ or greater is chosen, primarily for the numerical purpose of avoiding the need for unreasonably small steps at early times

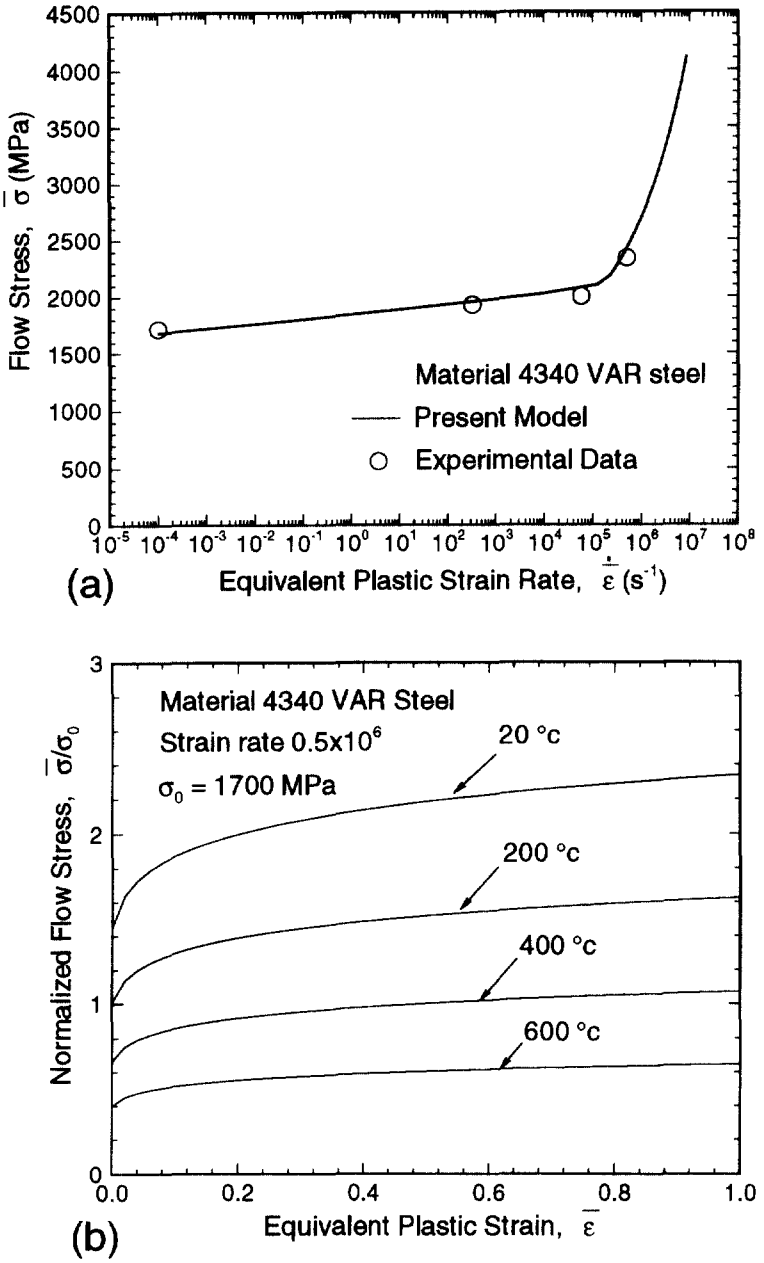

Fig. 1. Elastic–viscoplastic response of 4340 VAR steel employed in the numerical simulations. (a) Effect of equivalent plastic strain rate on the flow stress. (b) Effect of strain hardening and temperature on flow stress.

when the shear stresses are large. These stresses are relaxed in a few nanoseconds. The uncertainty in the response of the material at small strains and at large strain rates is unavoidable at the present because of the lack of experimental data in this regime. This uncertainty may have an effect on the calculated initial impact response of the material and is not expected to play a significant role in the evolution of plastic instability and the formation of shear bands since these events occur at much later times.

The material response of 4340 VAR steel is shown in Fig. 1, along with the plastic strain rate and the temperature dependence of the flow stress. The material parameters used in the model are listed in Table 1. To characterize the thermal softening behavior, the parameters β and k are chosen such that the stress-carrying capacity of each material almost vanishes when the temperature reaches more than 1000°C.

Table 1. Physical properties and material parameters used to describe the model for AISI 4340 VAR steel

$E = 202$ GPa, $\sigma_0 = 1700$ MPa
$m = 100.0$, $\beta = 4.75$
$c_p = 465$ J/(Kg K), $\alpha = 1.0 \times 10^5$ 1/K
$a = 10.0$, $\dot{\varepsilon}_0 = 1.0 \times 10^{-4}$ s^{-1}
$\dot{\varepsilon}_m = 5.0 \times 10^8$ s^{-1}, $\varepsilon_0 = 0.01$
$k = 100.0$ W/m K, $T_0 = 293$ K
$\kappa = 0.13$, $N = 0.1$, $\nu = 0.3$
Density = 7600 Kg/m^3
Longitudinal wave speed = 5983 m/s
Shear wave speed = 3154 m/s

3. FINITE ELEMENT IMPLEMENTATION

As discussed by Budiansky (1969), the principle of virtual work (10) can be used as the variational principle for a solid continuum undergoing arbitrarily large displacements and deformations. Moreover, the variational equation governing the thermo-mechanical energy balance can be obtained from the balance of energy, (27), as

$$\int_V \rho_0 c_p \dot{T} \delta T \, dV = \int_V \chi \tau : \mathbf{D}^p \delta T \, dV - \int_V Jk(\mathbf{F}^{-1} \cdot \mathbf{F}^{-T} \cdot \nabla_0)(\nabla_0 \cdot \delta T) \, dV. + \int_S Jk\mathbf{N} \cdot \{(\mathbf{F}^{-1} \cdot \mathbf{F}^{-T} \cdot \nabla_0 T)\} \delta T \, dS \quad (45)$$

When the finite-element approximations for the displacement and temperature fields are substituted into (10) and (45), the resulting equations take the form

$$\mathbf{M} \frac{\partial^2 \mathbf{U}}{\partial t^2} = \mathbf{R}, \quad (46)$$

$$\mathbf{C} \frac{\partial T}{\partial t} = -\mathbf{K}\mathbf{T} + \mathbf{H}, \quad (47)$$

where $\mathbf{U}$ is the vector of nodal displacements, $\mathbf{T}$ is the vector of nodal temperatures, $\mathbf{M}$, $\mathbf{C}$, $\mathbf{K}$, are, respectively, the mass, heat capacitance, and heat conductance matrices, and $\mathbf{R}$ and $\mathbf{H}$ are the mechanical and thermal force vectors. A lumped mass matrix is used in (46) instead of the consistent mass matrix; the lumped mass matrix has been found preferable for explicit time integration procedures from the point of view of computational efficiency and accuracy (Krieg and Key, 1973). Additionally, a lumped heat capacitance matrix is used in the (47).

An explicit time integration scheme based on the Newmark β-method, with $\beta = 0$, and $\gamma = 0.5$ (Belytschko *et al.*, 1976) is used to integrate the equations of motion to obtain the nodal velocities and nodal displacements via

$$\frac{\partial^2 \mathbf{U}^{n+1}}{\partial t^2} = \mathbf{M}^{-1} \mathbf{R}^{n+1}, \quad (48)$$

$$\frac{\partial \mathbf{U}^{n+1}}{\partial t} = \frac{\partial \mathbf{U}^n}{\partial t} + \frac{1}{2} \Delta t_n \left(\frac{\partial^2 \mathbf{U}^n}{\partial t^2} + \frac{\partial^2 \mathbf{U}^{n-1}}{\partial t^2} \right), \quad (49)$$

$$\mathbf{U}^{n+1} = \mathbf{U}^n + \Delta t_n \frac{\partial \mathbf{U}^n}{\partial t} + \frac{1}{2}(\Delta t_n)^2 \frac{\partial^2 \mathbf{U}^n}{\partial t^2}, \tag{50}$$

where $(\,)^{-1}$ denotes the matrix inverse.

The plastic dissipation rate, $\boldsymbol{\tau} : \mathbf{D}^p$, is calculated and its contribution to the thermal force vector, $\mathbf{H}^n$, is determined. The nodal temperature at t_{n+1} are obtained via

$$\frac{\partial T^{n+1}}{\partial t} = \mathbf{C}^{-1}(-\mathbf{K}^n T^n + \mathbf{H}^n), \tag{51}$$

and

$$T^{n+1} = T^n + \Delta t_n \frac{\partial T^{n+1}}{\partial t}. \tag{52}$$

The rate tangent modulus expansion method (Peirce *et al.*, 1984) is used to update the contravariant components of the convected Kirchhoff stress tensor, i.e.

$$\tau^{n+1} = \tau^n + \dot{\tau}^c \Delta t_n. \tag{53}$$

Following this model, the equivalent plastic strain is expressed as a linear combination of its values at t_n and t_{n+1},

$$\dot{\bar{\varepsilon}} = (1-\theta)\dot{\bar{\varepsilon}}^n + \theta \dot{\bar{\varepsilon}}^{n+1} \quad 0 \leqslant \theta \leqslant 1, \tag{54}$$

with $\dot{\bar{\varepsilon}}^{n+1}$, approximated by a first order Taylor series expansion in $\bar{\sigma}$, $\bar{\varepsilon}$ and T as

$$\dot{\bar{\varepsilon}}^{n+1} = \dot{\bar{\varepsilon}}^n + \Delta t_n \left[\left.\frac{\partial \dot{\bar{\varepsilon}}}{\partial \bar{\sigma}}\right|_n \dot{\bar{\sigma}} + \left.\frac{\partial \dot{\bar{\varepsilon}}}{\partial \bar{\varepsilon}}\right|_n \dot{\bar{\varepsilon}} + \left.\frac{\partial \dot{\bar{\varepsilon}}}{\partial T}\right|_n \dot{T} \right]. \tag{55}$$

Using J_2 flow theory, $\dot{\bar{\sigma}}$ can be expressed as

$$\dot{\bar{\sigma}} = \mathbf{p} : \mathscr{L}^e : \mathbf{D} - 3G\dot{\bar{\varepsilon}}. \tag{56}$$

Substituting (55) and (56) into (54) gives the equivalent plastic strain rate as

$$\dot{\bar{\varepsilon}} = \frac{\dot{\bar{\varepsilon}}^n}{1+\zeta} + \frac{\zeta}{(1+\zeta)} \frac{1}{\mathrm{H}} \left(\mathbf{p} : \mathscr{L}^e : \mathbf{D} + \dot{T} \frac{\partial \dot{\bar{\varepsilon}}/\partial T}{\partial \dot{\bar{\varepsilon}}/\partial \bar{\sigma}} \right), \tag{57}$$

where

$$\zeta = \theta \Delta t_n \frac{\partial \dot{\bar{\varepsilon}}}{\partial \bar{\sigma}} H, \quad \text{and} \quad H = 3G - \frac{\partial \dot{\bar{\varepsilon}}/\partial \bar{\varepsilon}}{\partial \dot{\bar{\varepsilon}}/\partial \bar{\sigma}}. \tag{58}$$

The derivatives used in (57) and (58) can be obtained from eqns (42)–(44).

The Jaumann rate of Kirchhoff stress is obtained by using eqns (40), (41) and (57) in (34) as

$$\overset{\nabla}{\boldsymbol{\tau}} = \left[\mathscr{L}^e - \frac{\zeta}{1+\zeta} \frac{(\mathscr{L}^e : \mathbf{p}) \otimes (\mathscr{L}^e : \mathbf{p})}{H} \right] : \mathbf{D} - \frac{1}{1+\zeta} \left[\dot{\bar{\varepsilon}} + \frac{\zeta}{H} \frac{\partial \dot{\bar{\varepsilon}}/\partial T}{\partial \dot{\bar{\varepsilon}}/\partial \bar{\sigma}} \dot{T} \right] \frac{3G}{\bar{\sigma}} \boldsymbol{\tau} - \alpha \dot{T}(2G + 3\lambda)\mathbf{I}. \tag{59}$$

The specific problem considered here is plane strain, in-plane shear loading of a rectangular pre-notched specimen, as shown in Fig. 2(a). A Cartesian coordinate system with the origin placed at the notch tip is used as reference. The in-plane shear loading is aligned with positive y^2 direction with the y^1–y^2 plane being the plane of deformation. The initial and boundary conditions can be written as

$$\begin{aligned}
&f^1 = 0, \quad f^2 = 0 \quad \text{on } y^1 = -w_1 \\
&f^1 = 0, \quad f^2 = 0 \quad \text{on } y^1 = w_2 \\
&f^1 = 0, \quad f^2 = 0 \quad \text{on } y^2 = 0 \quad \text{and} \quad y^1 < 0 \\
&f^1 = 0, \quad f^2 = 0 \quad \text{on } y^2 = -b_2 \\
&u^1 = \int_0^t V(t)\,\mathrm{d}t \quad f^2 = 0 \quad \text{on } y^2 = b_1.
\end{aligned} \tag{60}$$

The function $V(t)$ in (60) is taken to increase smoothly from time $t = 0$ according to

$$V(t) = \begin{cases} V_0/t_{\text{rise}}, & \text{for } t \leqslant t_{\text{rise}}, \\ V_0, & \text{for } t_{\text{rise}} < t \leqslant t_{\text{fall}} \end{cases} \tag{61}$$

with V_0 being the prescribed shear velocity. The duration of the shear pulse is taken to be 1 μs with rise time and fall time being equal to 100 ns. A $V_0 = 35$ m/s is used in (61) for all finite element simulations described in the present paper. This magnitude of V_0 assures that the stresses in the bulk of the specimen remain below the Hugoniot Elastic Limit (HEL) of the particular 4340 VAR steel being investigated and all inelasticity is confined to a small region ahead of the notch. The specimen dimensions are taken as $w_1 = w_2 = 16.0$ mm and $b_1 = b_2 = 3.5$ mm. These dimensions assure that no wave reflections from the specimen boundaries arrive at the central part of the specimen, i.e. the region in the vicinity of the notch tip, for the entire duration of the loading pulse.

The finite element mesh used for the computational experiments is shown in Fig. 2(b). Figure 2(c) shows the mesh in the vicinity of the notch tip. The initial notch tip is semi-circular with a diameter of 10 μm. The region ahead of the notch consists of a uniform mesh with 24 quadrilaterals in the y^1 direction and six quadrilaterals placed symmetrically about the y^1 axis and parallel to the y^2 direction. Each quadrilateral element in the uniform mesh zone has a dimension of 10×10 μm. The entire finite-element mesh consists of 2430 quadrilateral elements with 9980 degrees of freedom.

The finite element discretization is based on linear displacement triangular elements that are arranged in a "crossed-triangle" quadrilateral pattern. In these constant strain triangular sub-elements the displacements and temperature are taken to vary linearly over the triangular elements. Nagtegaal *et al.* (1974) have shown that an element of this type can accommodate isochoric deformations. This is of significance since plastic strain is volume preserving, so that the total deformation at large strains is nearly isochoric. Another reason for using the crossed-triangle elements in the present context stems from the need to resolve localized shear bands. As discussed by Tvergaard *et al.* (1981), a mesh composed of crossed triangles can resolve narrow shear bands in four dimensions—parallel with either the sides or the diagonals of the element. In presenting computational results, the quadrilateral is regarded as the basic element, and when reporting values of field quantities the average value of the four triangles is associated with the centroid of the quadrilateral.

4. RESULTS AND DISCUSSION

In the present paper results of computational experiments, based on five different material models, are presented. As a base material the material parameters corresponding to 4340 VAR steel are chosen. The parameters for the second material [Material Model

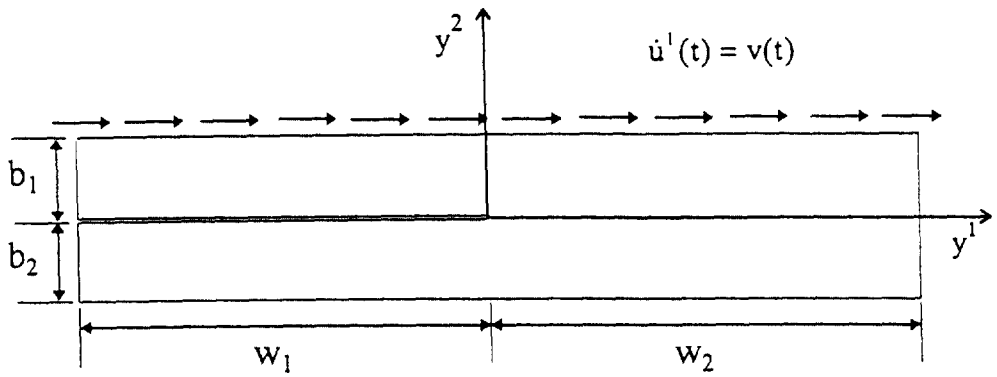

(a)

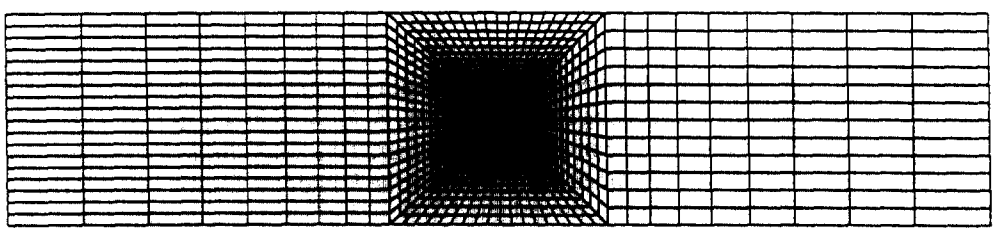

(b)

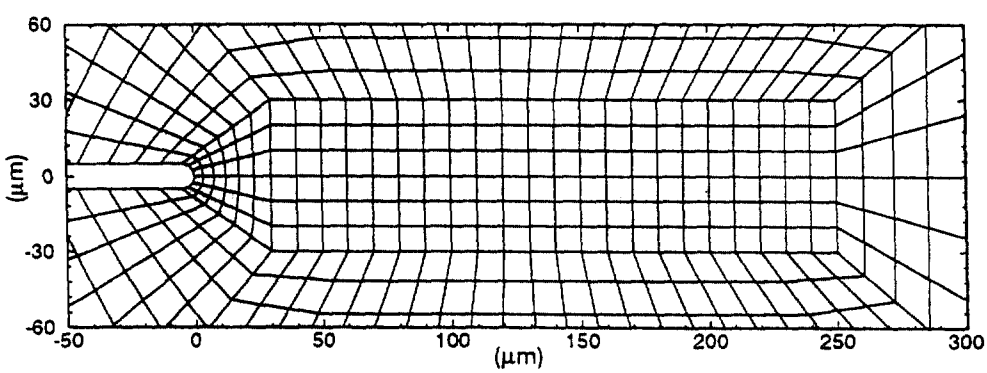

(c)

Fig. 2. (a) Schematic of the specimen configuration. (b) Finite element discretization of the specimen configuration. (c) Finite element mesh in the vicinity of the notch tip (also referred to as the process zone). The diameter of the notch tip is 10 μm. Each quadrilateral element comprises four "crossed" triangle sub-elements. Dimension of the quadrilateral elements in the process zone is 10×10 μm.

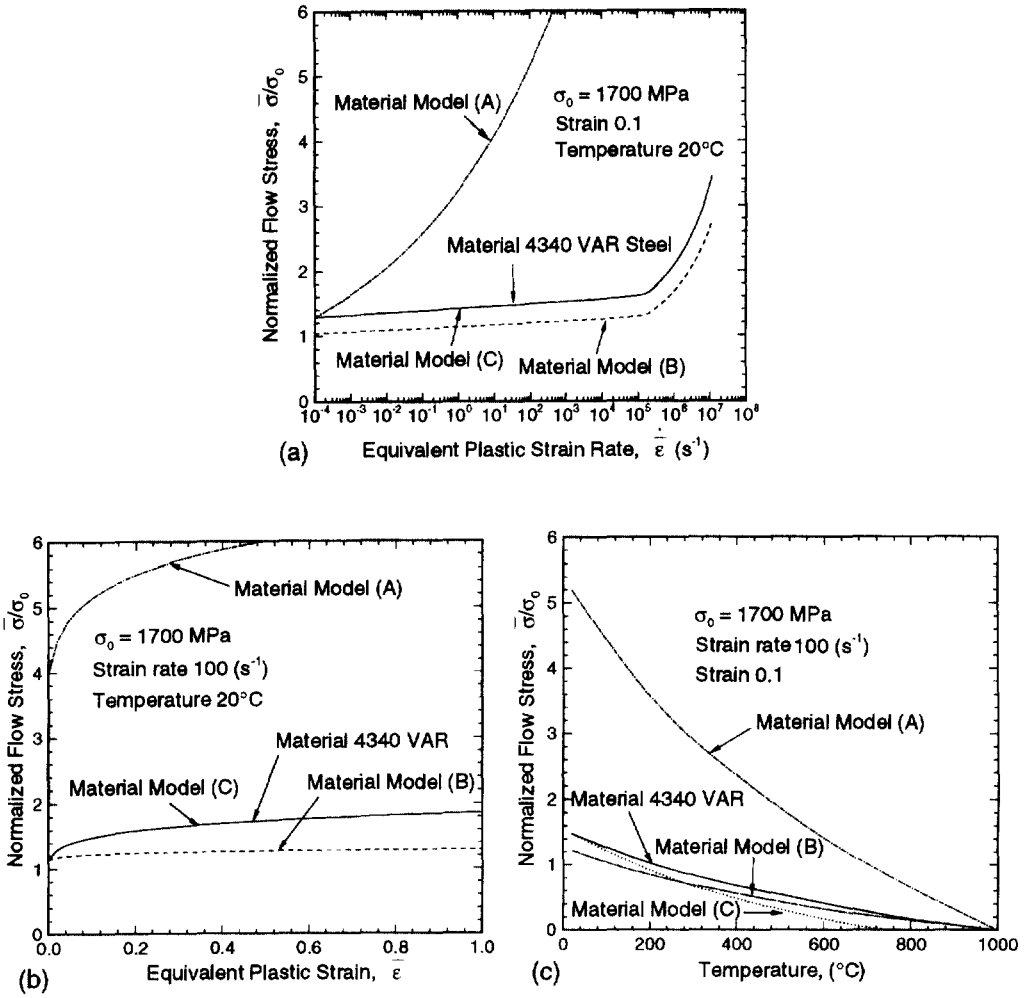

Fig. 3. Material models employed in the numerical simulations. For Material Model (A), strain rate sensitivity parameter m is changed from 100–10. For Material Model (B), strain hardening coefficient n is changed from 0.1–0.025. For Material Model (C), thermal softening parameter β is changed from 4.75–5.92. (a) Effect of equivalent plastic strain rate on flow stress. (b) Strain hardening characteristics. (c) Thermal softening characteristics.

(A)] are the same as those of the base material except that the material strain–rate sensitivity parameter m is changed from 100–10. This value of m provides enhanced material strain rate sensitivity and its effect on the flow stress is shown in Fig. 3(a). For the third material [Material Model (B)], the strain hardening exponent is changed from 0.1 to 0.025. Decreasing the strain hardening exponent results in a near perfectly plastic material response, as shown in Fig. 3(b). For the fourth material [Material Model (C)], an enhanced thermal softening material response is employed to investigate the sensitivity of shearing deformation to accelerated decrease in flow stress due to temperature rise. This is achieved by increasing the magnitude of the parameter β in (44) from 4.75 to 5.92. The corresponding variation of flow stress with temperature is shown in Fig. 3(c). Also, results are presented for the 4340 VAR steel with negligible heat conduction to investigate the effects of adiabatic conditions on the evolution of plastic instability.

4.1. *Initiation and propagation of plastic instability*

(*a*) 4340 *VAR steel.* Figure 4(a–d) represent contour plots summarizing the mechanical and thermal fields in the vicinity of the region undergoing plastic deformation, obtained 900 ns after the arrival of the shear loading pulse at the notch plane. The applied loading corresponds to a purely tangential particle velocity history with a shear stress amplitude of

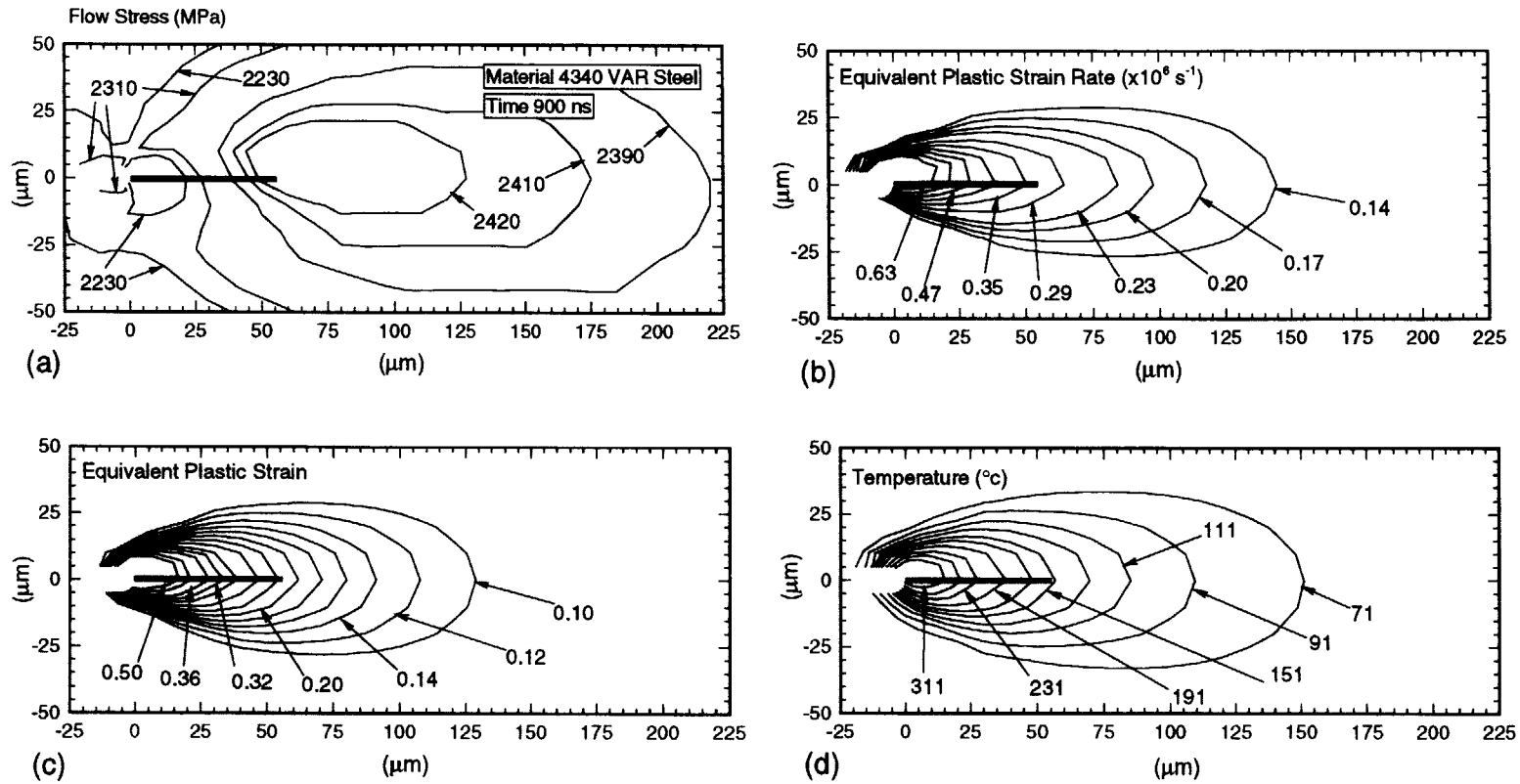

Fig. 4. Mechanical and thermal fields in the vicinity of notch tip region at 900 ns after the arrival of the shear wave at the notch plane for 4340 VAR steel. (a) Flow stress distribution. (b) Equivalent plastic strain rate distribution. (c) Plastic strain distribution. (d) Temperature distribution.

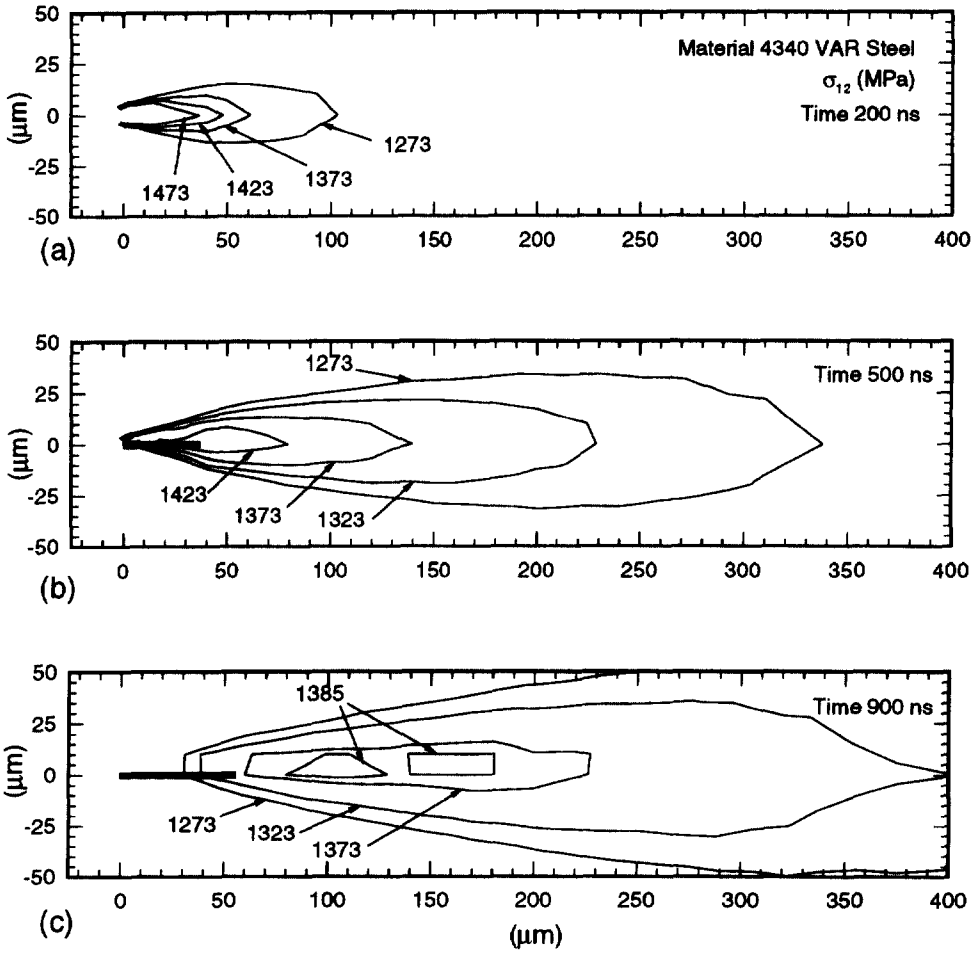

Fig. 5. Distribution of shear stress σ_{12} at three different times after the arrival of the shear wave at the notch plane for 4340 VAR steel. (a) $t = 200$ ns. (b) $t = 500$ ns. (c) $t = 900$ ns.

850 MPa and a duration of 1000 μs. These fan shaped two-dimensional local mechanical and thermal fields govern the initiation and progression of the plastic instability under the applied loading. The solid horizontal line emanating from the origin represents the distance plastic instability has extended to from its initial position during the 900 ns time interval. The plots indicate that the gradients in flow stress, the equivalent plastic strain rate, the plastic strain and temperature increase as we move towards the notch tip along the y^1 direction and also as we approach the notch plane along the y^2 direction. This distribution of the mechanical and the thermal fields is consistent with the localization of shearing deformation along the notch plane.

Also, the initiation and propagation of plastic instability depends on the intensity of shear stresses, σ_{12}, in the vicinity of the region undergoing plastic localization. The intensity of the shear stresses affects the rate of plastic deformation of material elements in the process zone and reflects the material resistance to the propagation of the plastic instability. Figure 5(a–c) shows a sequence of the shear stress distributions in the region directly ahead of the notch tip at three different time intervals after the arrival of the shear loading pulse at the notch plane, i.e. at $t = 200$, 500 and 900 ns. From these plots it is observed that during the initiation and propagation of the plastic shear instability, the shear stress distribution is approximately symmetric with respect to the notch plane. The shear stresses are highest along the centerline (notch plane) and decrease rapidly as we move away in a direction perpendicular to the notch plane. Also, Fig. 5(b) and (c) indicate that the shear stresses increase rapidly as we move away from the tip of the localized region in the positive y_1 direction along the notch plane, reaches a maximum and then decreases to an almost

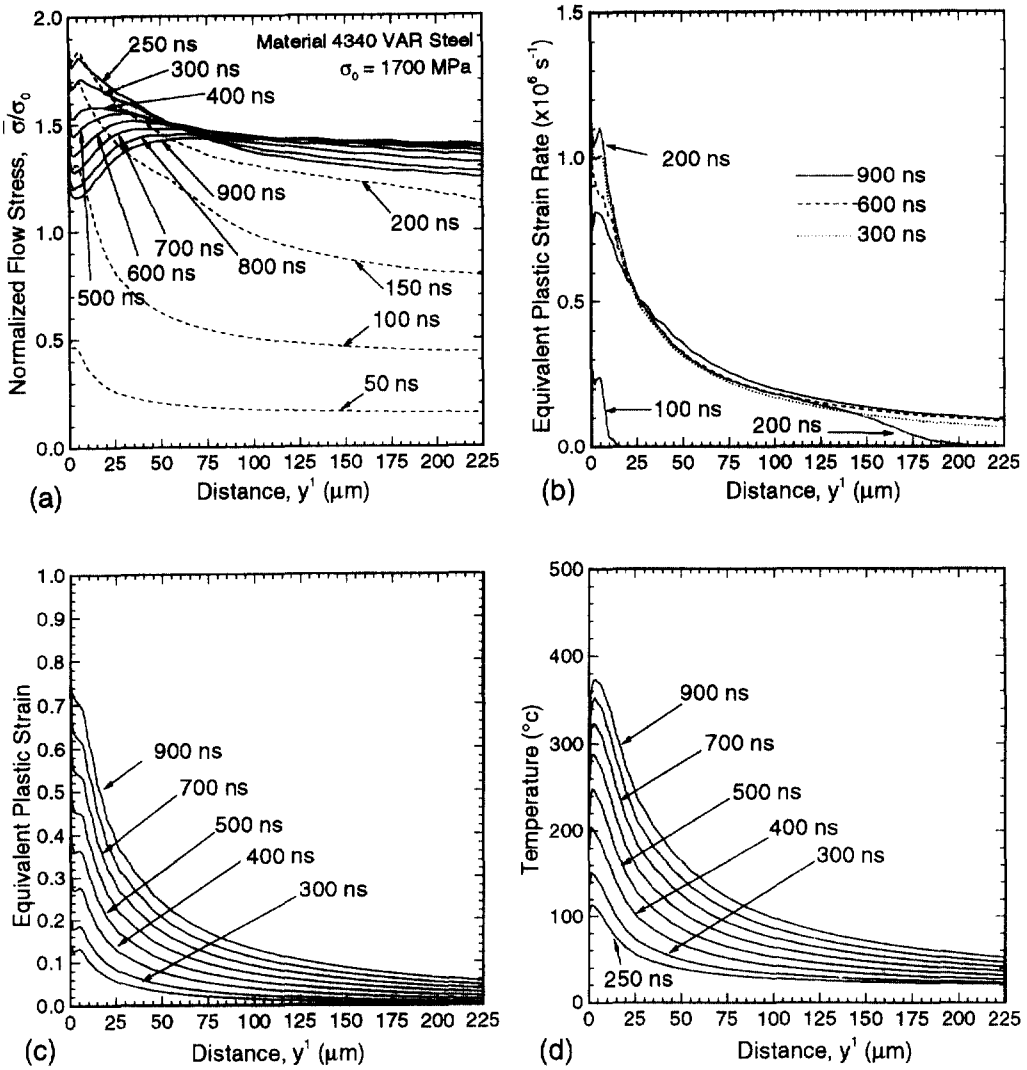

Fig. 6. Evolution of mechanical and thermal fields as a function of distance along the loading axis (y^1 axis) after the arrival of the shear wave at the notch plane for 4340 VAR steel. (a) Normalized flow stress. (b) Equivalent plastic strain rate. (c) Equivalent plastic strain. (d) Temperature.

uniform shear stress region. The size of this uniform shear stress region is relatively small initially. But, as the plastic instability propagates the size of this region increases, reaching a maximum at $t = 900$ ns. These general features are consistent with the observations of Zhou *et al.* (1996b) and the concept of an active shear process zone at the tip of the propagating shear band proposed by Grady (1992, 1994).

The deformation and temperature fields for the case of propagating plastic shear instabilities are different from one-dimensional localized bands in that they are non-uniform along as well as across the localized regions. The mechanical and thermal fields, in a direction along and perpendicular to the notch plane are shown in Figs 6(a–d) and 7(a–d). The initiation and the subsequent progression of plastic instability is best understood from Fig. 6(a), which shows the variation of the flow stress as a function of distance from the notch tip, at various time intervals. The plot is obtained from Fig. 4(a) by using the line extraction option available in the commercial plotting package TECPLOT®. The ordinate of Fig. 6(a) is normalized with respect to the initial flow stress, σ_0, for 4340 VAR steel (Table 1). Upon the arrival of the incident shear pulse at the notch plane, the flow stress of the material ahead of the notch tip increases steadily for approximately 250 ns due to strain hardening and the strain rate sensitivity of 4340 VAR steel. At the same time, due to

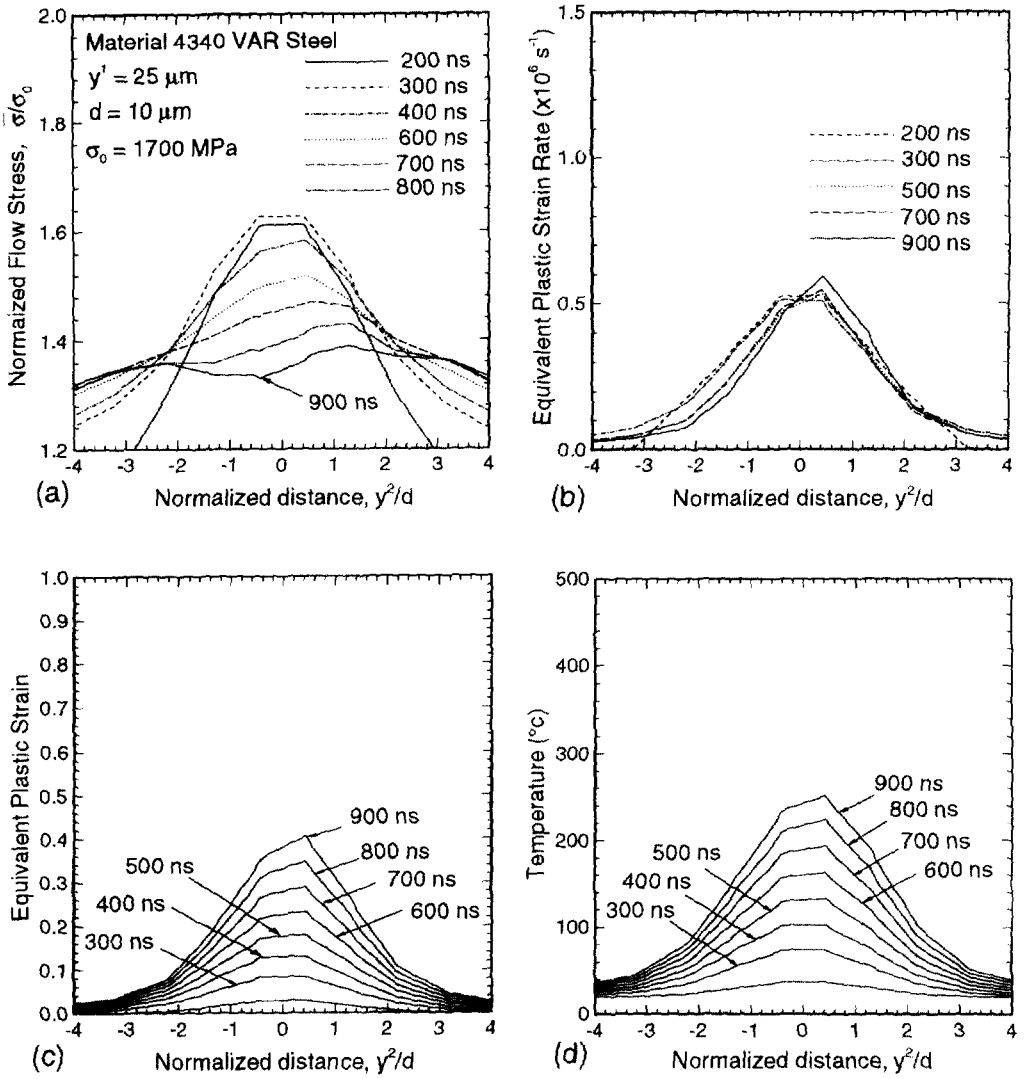

Fig. 7. Evolution of mechanical and thermal fields at $y^1 = 25\ \mu m$ and as a function of normalized distance along the y^2 axis after the arrival of the shear wave at the notch plane for 4340 VAR steel (d-notch diameter). (a) Normalized flow stress. (b) Equivalent plastic strain rate. (c) Equivalent plastic strain. (d) Temperature.

thermo-mechanical coupling and the relatively short time available for heat conduction, the temperature at these material points starts to increase rapidly. The resulting thermal softening plays an important role in the evolution of the plastic instability. When the elevation of flow stress due to strain hardening and the rate sensitivity of the material is offset by the effect of thermal softening on the flow stress, the condition of plastic instability is initiated. This information is obtained from Fig 6(a) by identifying, for a particular material element, the time at which the rate of increase of flow stress becomes negative. It should be noted that although this criterion is not a sufficient condition for shear band localization (Clifton *et al.*, 1984), it should still be acceptable for the purposes of the present analysis in identifying the initiation and propagation of plastic instability. Figure 7(a) shows the evolution of the flow stress as a function of distance along the y^2 coordinate axis and at a distance $y^1 = 25\ \mu m$ ahead of the notch tip. The flow stress increases to a level of approximately 1.8 times its initial level during the initial 250 ns, with maximum occurring along the notch plane, i.e. $y^2 = 0$, and then decreases as the effects of thermal softening start to dominate the effects of strain hardening and rate sensitivity of 4340 VAR steel.

Figures 6(b) and 7(b) show the evolution of the equivalent plastic strain-rate as a function of distance ahead of notch tip. For material elements in the immediate vicinity of

the notch tip, during the initial 250 ns, the equivalent plastic strain rate increases rapidly and attains a maximum of approximately 1.1×10^6 s^{-1}. This maximum in the equivalent plastic strain rate occurs before the initiation of the plastic instability, and then it actually decreases as the localization of the plastic instability occurs. Figure 8(a) and (b) depict the total equivalent strain rate (defined by $\sqrt{2/3}\mathbf{D}:\mathbf{D}$) as a function of distance y^1 at $y^2 = 0$, and as a function of y^2 at $y^1 = 25$ μm, respectively, for 4340 VAR steel. The total equivalent strain rate is observed to increase continuously with the applied shearing deformation, reaching a maximum of approximately 2×10^6 s^{-1} at $t = 900$ ns in the vicinity of the notch tip. Figure 8(c) and (d) show the corresponding variation of the equivalent thermal strain rate (defined by $\sqrt{2/3}\mathbf{D}^T:\mathbf{D}^T$ with $\mathbf{D}^T = \alpha\dot{T}\mathbf{I}$) as a function of distance y^1 at $y^2 = 0$ and y^2 at $y^1 = 25$ μm, respectively. Due to the relatively small magnitude of the equivalent thermal strain rate as compared to the equivalent plastic strain rate (shown in Figs 6(b) and 7(b)), the equivalent thermal strain rate has negligible effect on the total equivalent strain rate. Figure 8(e) and (f) show the variation of the equivalent elastic strain rate as a function of position y^1 at $y^2 = 0$, and y^2 at $y^1 = 25$ μm, respectively. These curves are obtained by subtracting the sum of the equivalent plastic strain rate and the equivalent thermal strain rate from the total equivalent strain rate. It is clearly observed from Fig. 8(e) and (f) that the equivalent elastic strain rate, after an initial decrease (from $t = 100$–200 ns), increases continuously with deformation leading to the dominance of the elastic strain rate in the region. This is in contrast to the previous shear band localization studies employing a power law strain-rate hardening material response in which the equivalent plastic strain rates have been reported to dominate the total equivalent strain-rate during the entire duration of the loading.

Figures 6(c), (d), 7(c) and (d) show the evolution of the equivalent plastic strain and temperature ahead of the notch tip as a function of time. Both the equivalent plastic strain and temperature increase monotonically with time at material points on either side (ahead and behind) of the plastic instability front. The continued plastic deformation/dissipation behind the tip of the plastically localized band is in contrast to the propagation of cracks where the crack faces separate and no further dissipation and deformation occurs behind the crack tip. The maximum plastic strain and the maximum temperature attained is as high as 0.8 and 375°C, respectively, in the immediate vicinity of the notch tip during the 900 ns time period. These higher values for strains and temperature are partly due to the longer durations of localized deformations present there. Also, from Fig. 7(c) and (d) it is observed that the plastic strains and temperature tends to localize in a narrow band ahead of the notch tip.

(*b*) 4340 *VAR steel* (*adiabatic case*). Figure 9(a–d) represent contour plots depicting the local mechanical and the thermal fields for 4340 VAR steel undergoing adiabatic deformation at time $t = 900$ ns. The solid horizontal line emanating from the origin represents the distance the plastic instability has extended from the notch tip during the 900 ns time interval. Figure 10(a–d) show the flow stress, the equivalent plastic strain-rate, the equivalent plastic strain, and temperature as a function of distance y^1 at $y^2 = 0$. From these plots it can be seen that the levels of flow stress (Fig. 9(a)) obtained for the adiabatic case are only slightly lower than those obtained for the heat conduction case. Also, the contours representing the plastic strain rate (Fig. 9(b)), the equivalent plastic strain (Fig. 9(c)) and temperature (Fig. 9(d)) for the adiabatic case are quite similar to those obtained for the heat conduction case. The propagation characteristics for plastic instability are also quite similar to the heat conduction case with the extension of the plastic instability being slightly greater for the adiabatic case. The similarity between the results for the heat conduction case and the adiabatic case is expected since the duration of these computational experiments is less than one microsecond allowing insufficient time for diffusion of heat away from the notch plane.

(*c*) *Effect of strain rate sensitivity* [*Material Model* (*A*)]. Figure 11(a–d) represent contour plots showing the local mechanical and the thermal fields for Material Model (A) in the vicinity of the notch tip at $t = 900$ ns. The solid horizontal line emanating from the

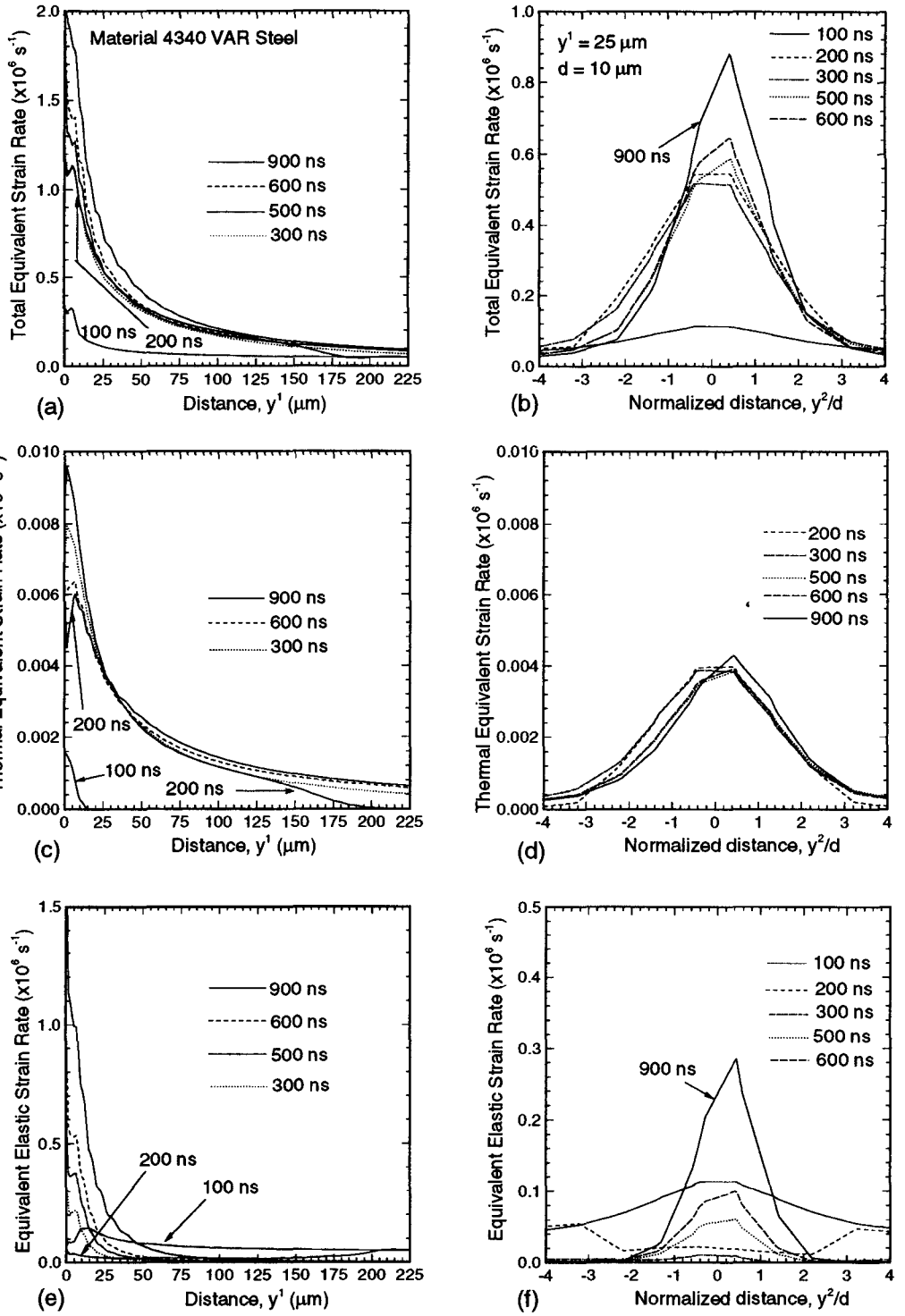

Fig. 8. Evolution of equivalent strain rate fields rate as a function of position y^1 at $y^2 = 0$ and y^2 at $y^1 = 25$ μm, respectively, after the arrival of the shear wave at the notch plane for 4340 VAR steel. (a) and (b) Total equivalent strain rate. (c) and (d) Thermal equivalent strain rate. (e) and (f) Equivalent elastic strain rate.

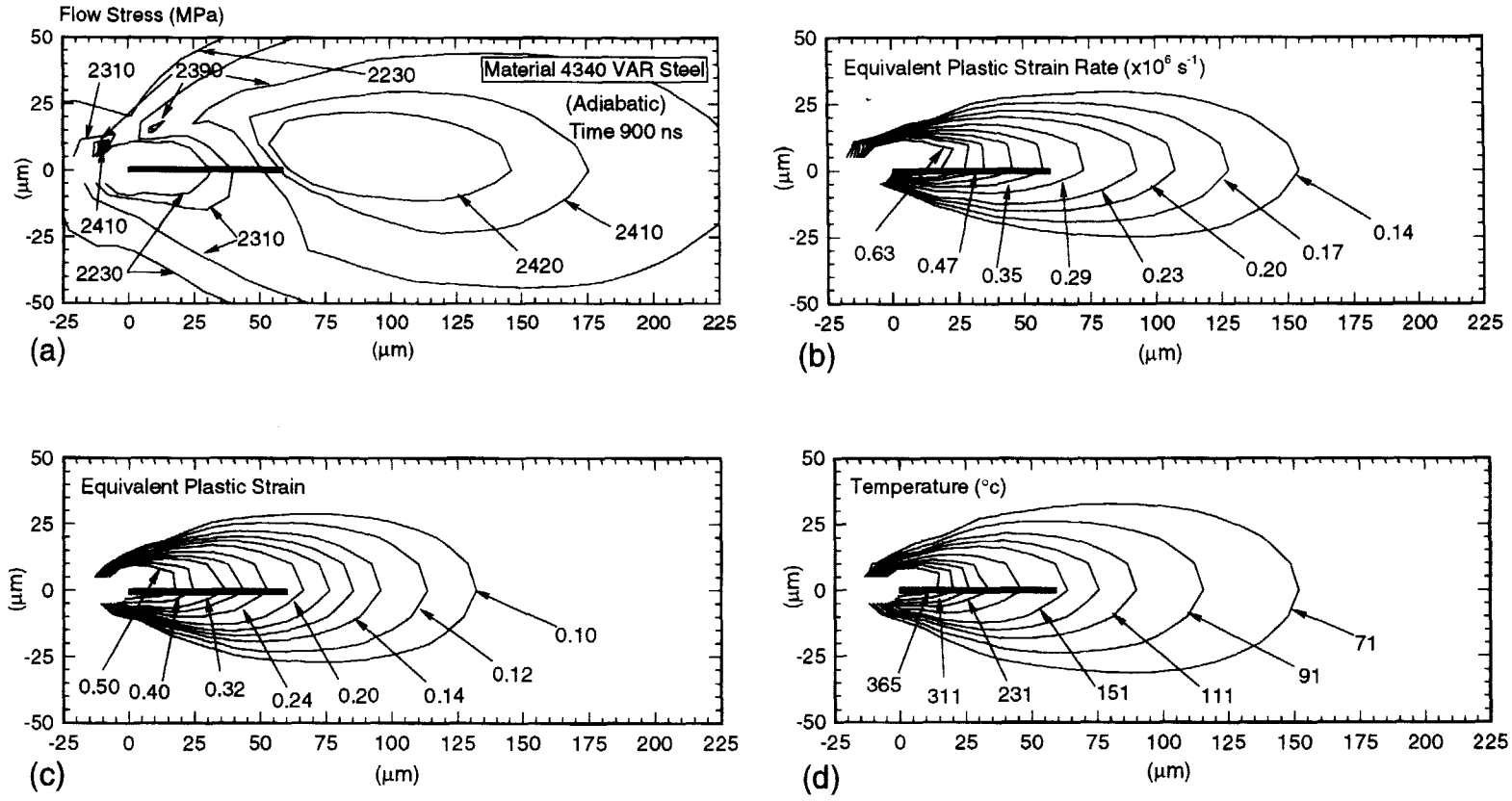

Fig. 9. Mechanical and thermal fields in the vicinity of notch tip region at 900 ns after the arrival of the shear wave at the notch plane for 4340 VAR steel (adiabatic case). (a) Flow stress distribution. (b) Equivalent plastic strain rate distribution. (c) Plastic strain distribution. (d) Temperature distribution.

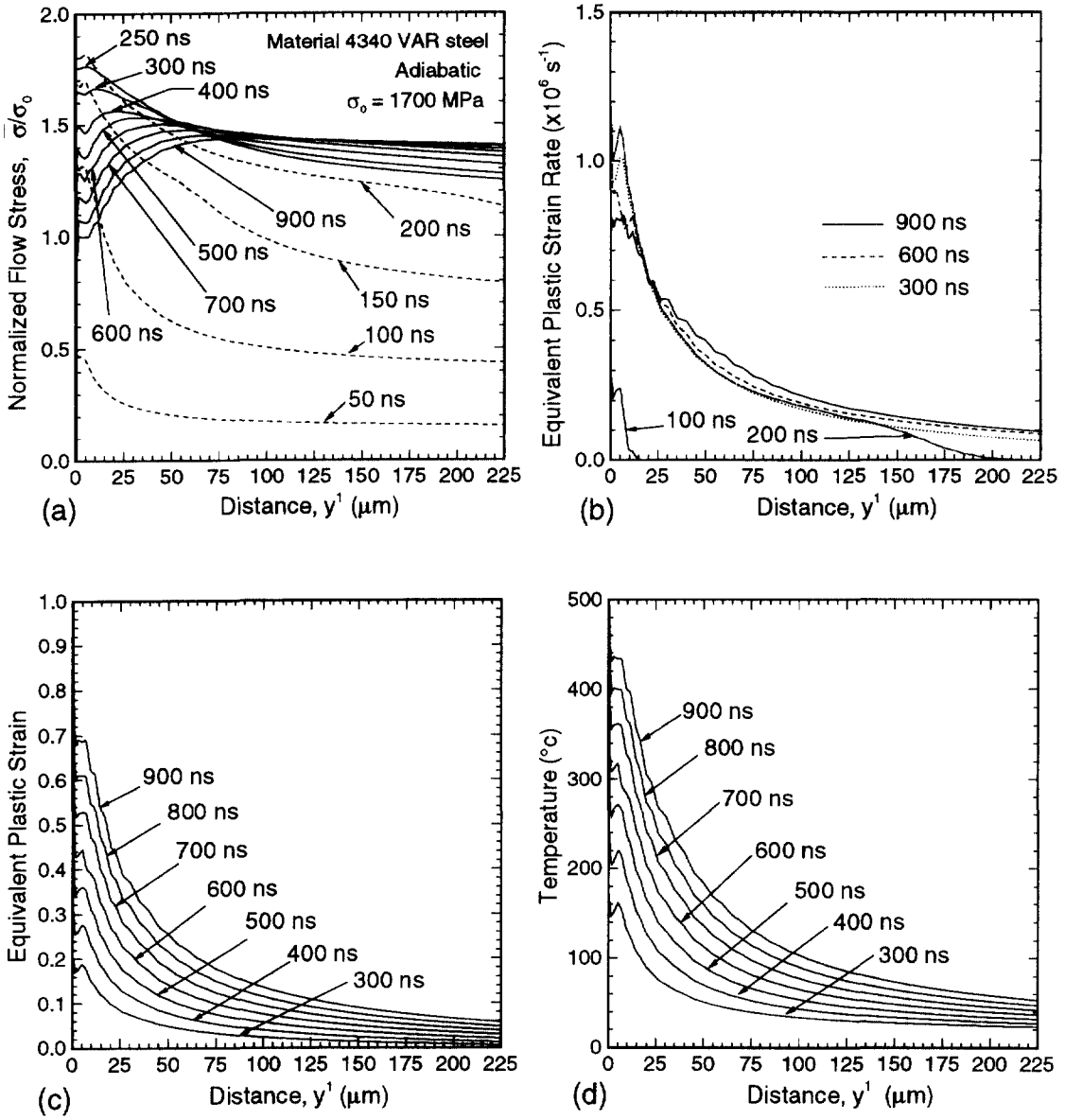

Fig. 10. Evolution of mechanical and thermal fields as a function of distance along the loading axis (y^1 axis) after the arrival of the shear wave at the notch plane for 4340 VAR steel (adiabatic case).

origin represents the distance plastic instability has extended from the notch tip during the duration of the shear loading pulse. Figure 12(a–d) show the flow stress, equivalent plastic strain-rate, equivalent plastic strain, and temperature as a function of distance ahead of the notch tip plotted on the undeformed configuration. Upon the arrival of the incident shear pulse the flow stress level ahead of the notch tip is increased significantly to $8\sigma_0$. This is primarily due to the strong material rate sensitivity inherent in Material Model (A). The magnitudes and the spatial distribution of the equivalent plastic strain rate, the equivalent plastic strain and temperatures are all drastically reduced as compared to the 4340 VAR steel case. These mechanical and thermal fields have a considerable effect on the localization of plastic instability. The initiation of the plastic instability is significantly delayed and the total extension of the plastic instability is only 16 μm.

(*d*) *Effect of straining hardening coefficient* [*Material Model* (*B*)]. Figure 13(a–d) show the contour plots summarizing the local mechanical and the thermal fields in the vicinity

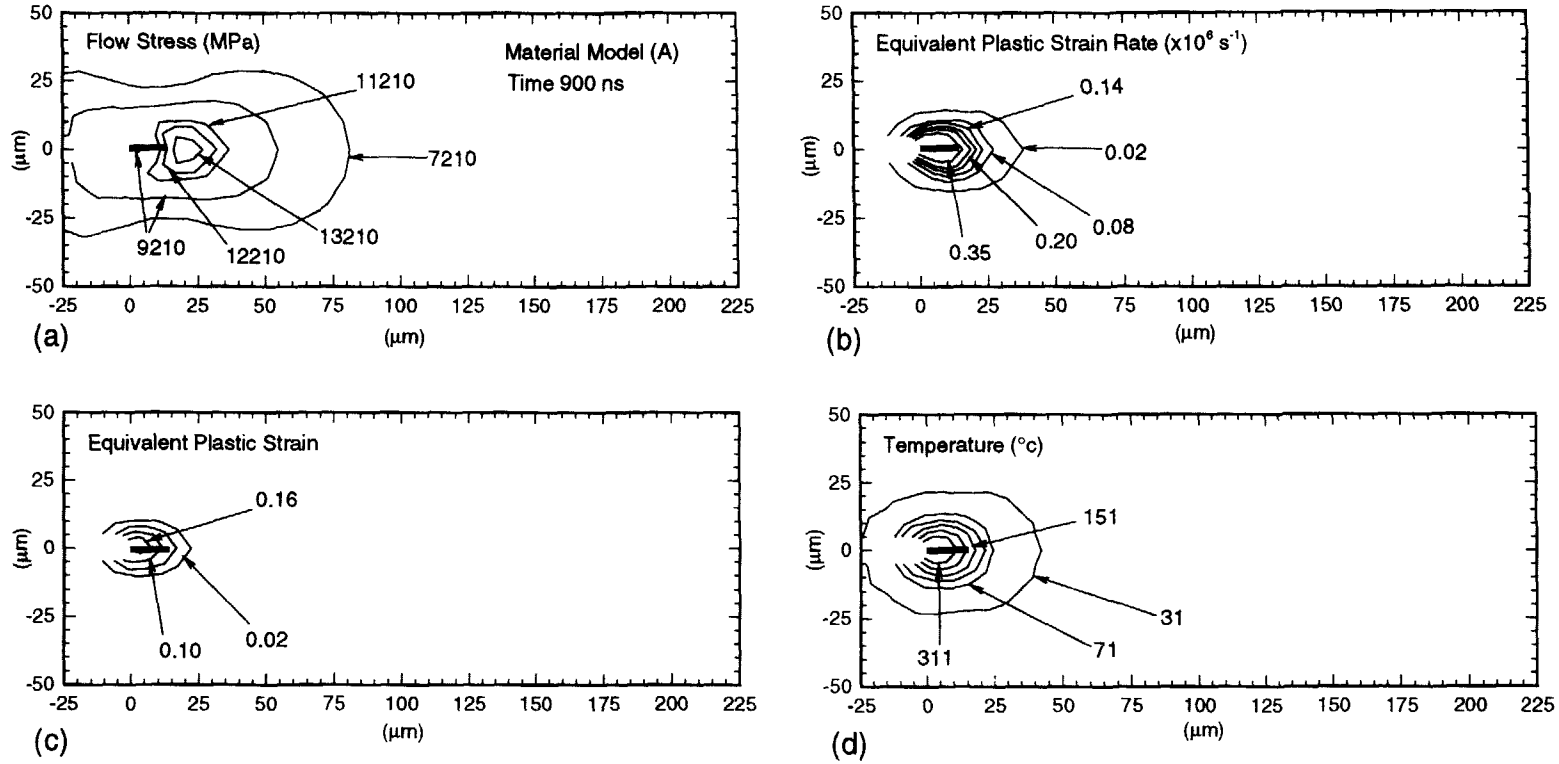

Fig. 11. Mechanical and thermal fields in the vicinity of notch tip region at 900 ns after the arrival of the shear wave at the notch plane for Material Model (A). (a) Flow stress distribution. (b) Equivalent plastic strain rate distribution (c) Plastic strain distribution. (d) Temperature distribution.

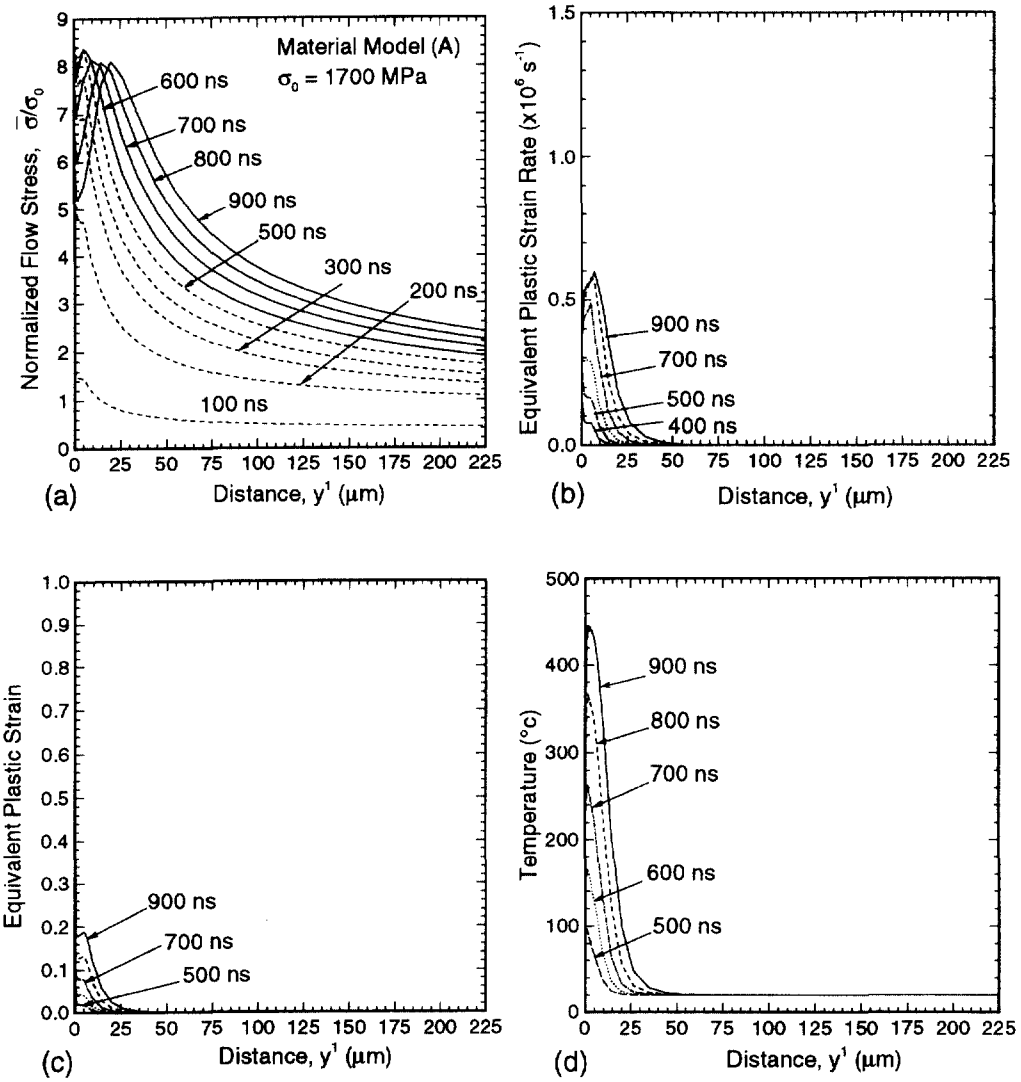

Fig. 12. Evolution of mechanical and thermal fields as a function of distance along the loading axis (y^1 axis) after the arrival of the shear wave at the notch plane for Material Model (A). (a) Normalized flow stress. (b) Equivalent plastic strain rate. (c) Equivalent plastic strain. (d) Temperature.

of the notch tip. The solid horizontal line emanating from the origin represents the distance plastic instability has extended from the notch tip during the duration of the shear loading pulse. Figure 14(a–d) show the flow stress, equivalent plastic strain-rate, equivalent plastic strain, and temperature as a function of distance ahead of the notch tip in the undeformed configuration. Lowering the strain hardening exponent has a dramatic effect on both the thermal and the mechanical fields. Although, the shape of the deformation and thermal fields are nearly identical to those obtained for the 4340 VAR steel, the various contour levels extend over a much larger distance from the notch. Also, the extension of the plastic instability is increased dramatically as compared to 4340 VAR steel. An important conclusion from these results is that if we want to develop material microstructures which are more susceptible to the spread of plastic localization it is desirable to design material microstructures with lower strain hardening characteristics and/or lower ultimate strengths.

(*e*) *Effect of thermal softening parameter* [*Material Model* (*C*)]. Figure 15(a–d) represent the contour plots showing the local mechanical and the thermal fields in the vicinity of the notch tip. The solid horizontal line emanating from the origin represents the distance the plastic instability has extended from the notch tip during the duration of the shear

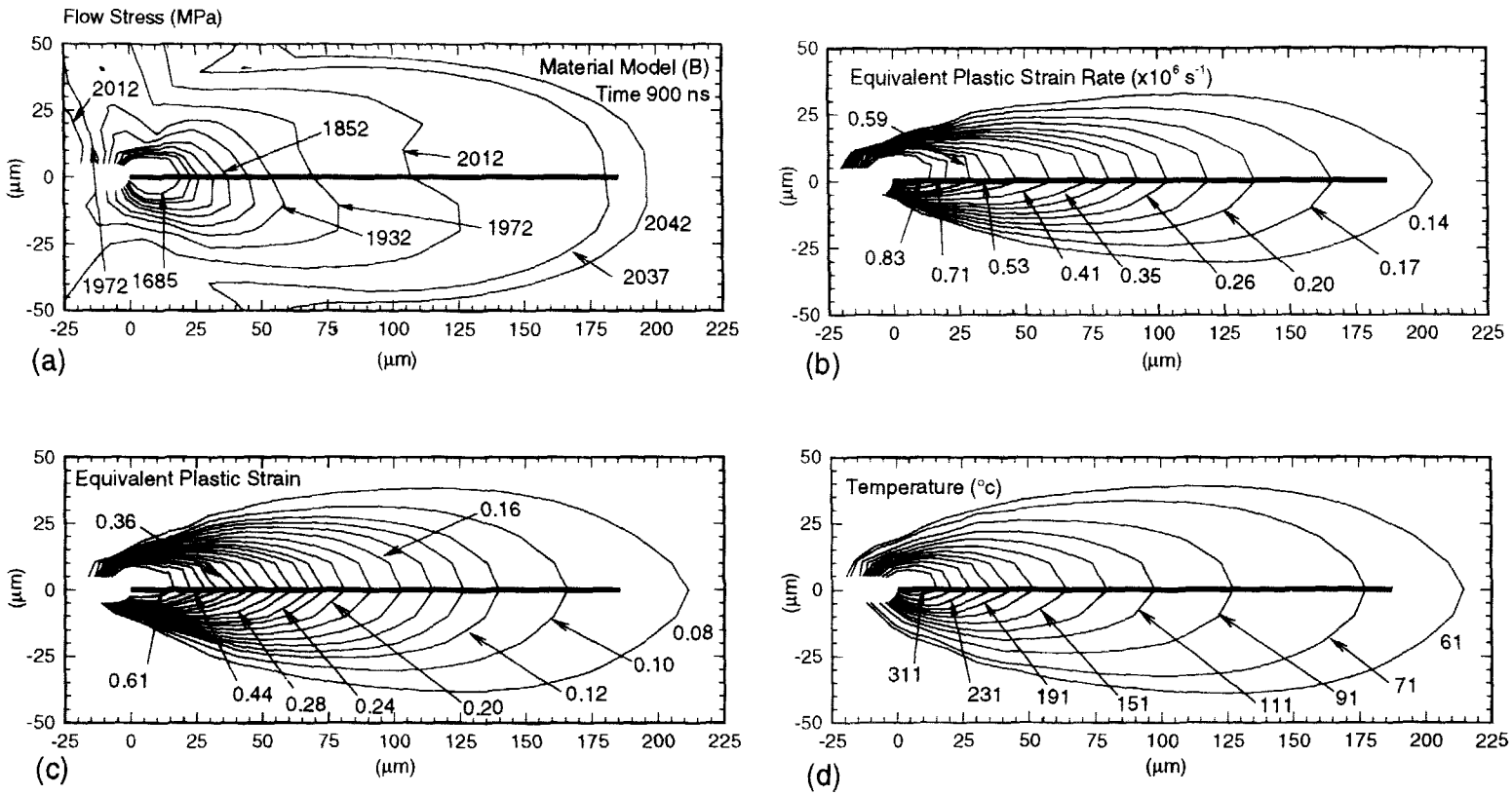

Fig. 13. Mechanical and thermal fields in the vicinity of notch tip region at 900 ns after the arrival of the shear wave at the notch plane for Material Model (B). (a) Flow stress distribution. (b) Equivalent plastic strain rate distribution. (c) Plastic strain distribution. (d) Temperature distribution.

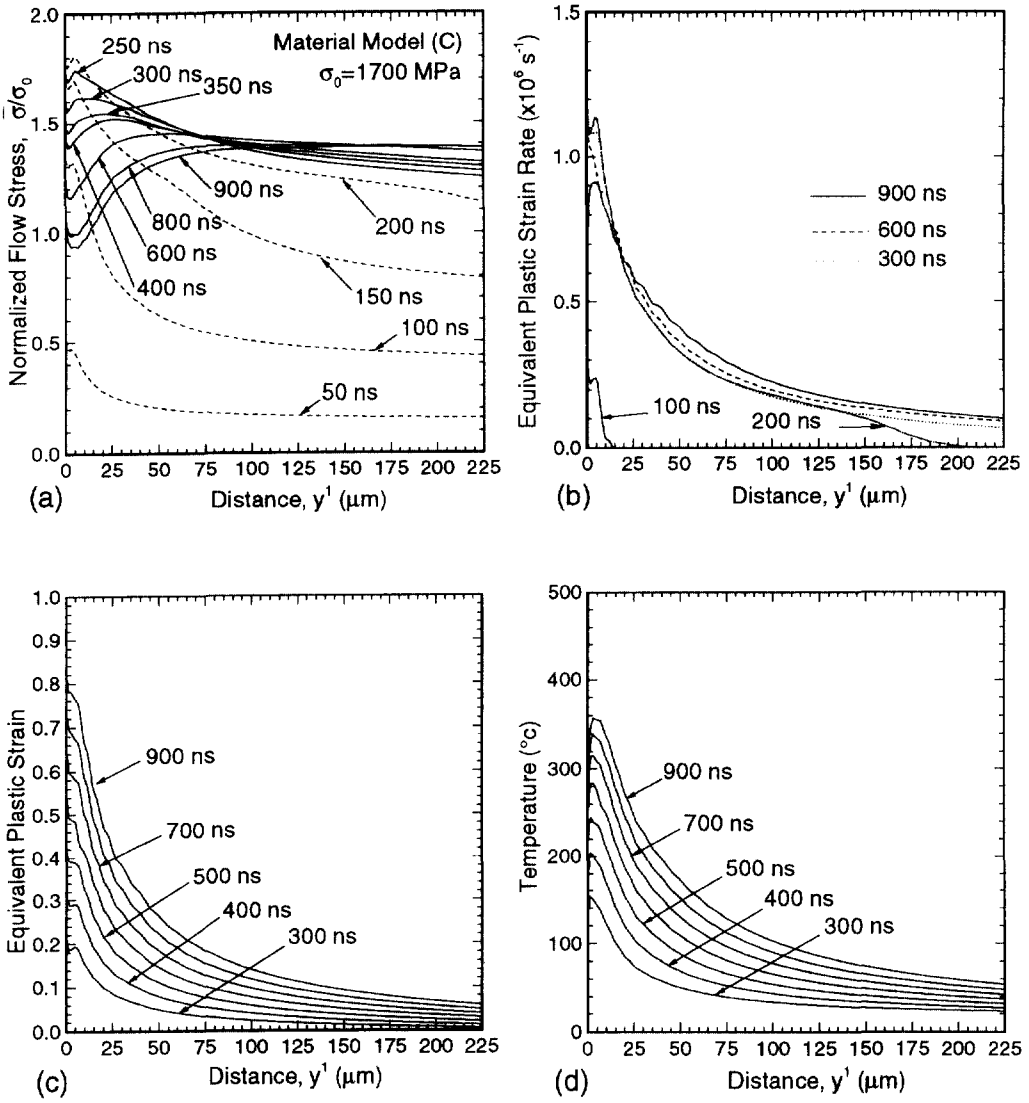

Fig. 14. Evolution of mechanical and thermal fields as a function of distance along the loading axis (y^1 axis) after the arrival of the shear wave at the notch plane for Material Model (B). (a) Normalized flow stress. (b) Equivalent plastic strain rate. (c) Equivalent plastic strain. (d) Temperature.

loading pulse. Figure 16(a–d) show the flow stress, equivalent plastic strain-rate, equivalent plastic strain, and temperature as a function of distance ahead of the notch tip in the undeformed configuration. From these figures it can be seen that increasing the thermal softening parameter β from 4.75 to 5.12 has a weak effect on the overall thermal and deformation characteristics as compared to the Material Model (A) and Material Model (B) cases. Also, the plastic instability propagation characteristics are quite similar to those observed in 4340 VAR steel with the plastic instability extension being only slightly greater.

4.2. *Extension history and speed of propagation of plastic instability*

The plastic instability extension history contains information about its dynamic characteristics including the time of initiation, the time of arrest and the speed of propagation. Figure 17 is a summary of the calculated length histories of propagating shear bands for 4340 VAR steel (heat conduction case), 4340 VAR steel (adiabatic case), Material Model (A), Material Model (B) and Material Model (C). The curves show a dramatic increase in length and speed of propagation of plastic instability for Material Model (B), which is assigned a reduced strain hardening parameter as compared to 4340 VAR steel. On the

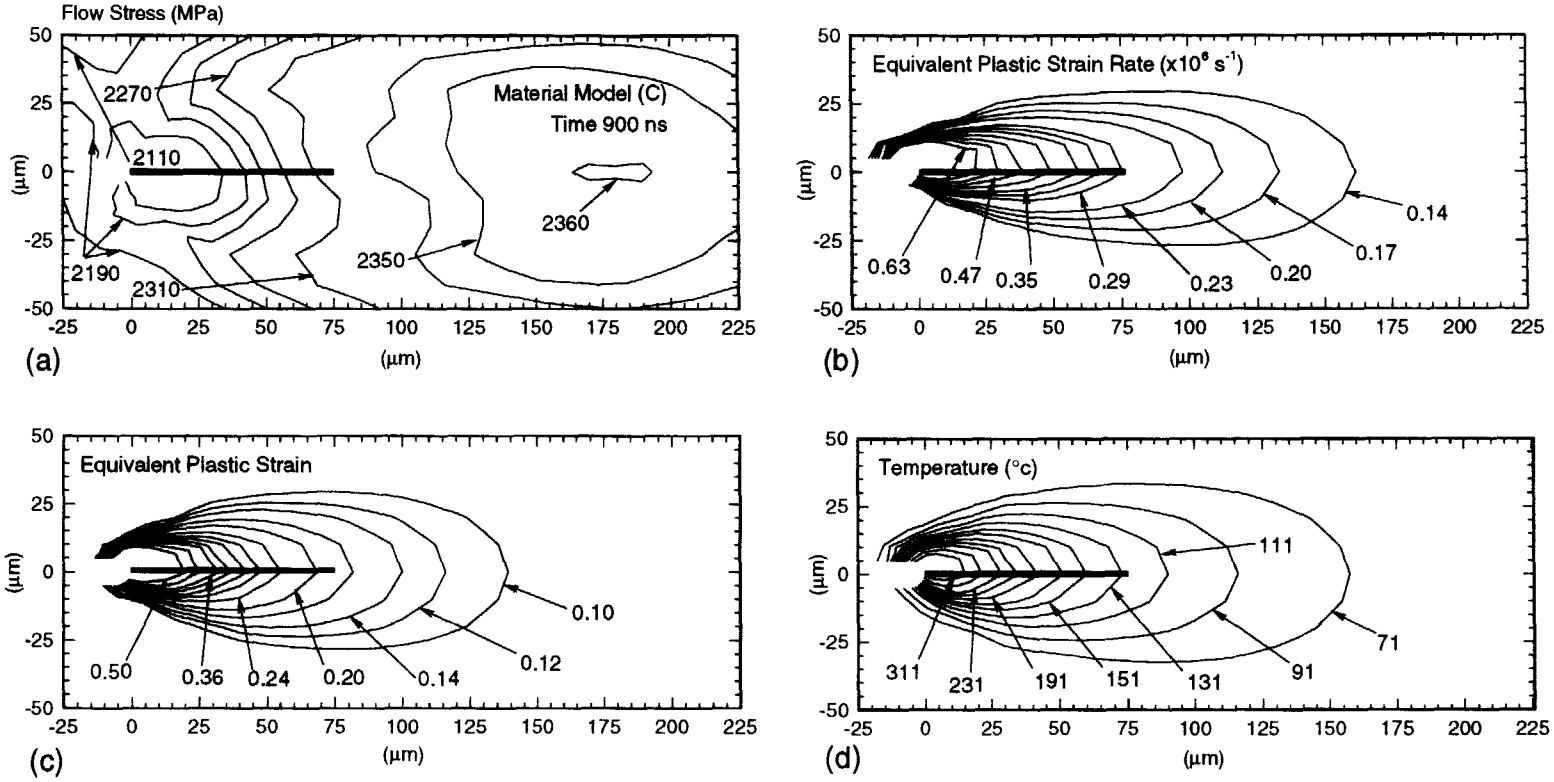

Fig. 15. Mechanical and thermal fields in the vicinity of notch tip region at 900 ns after the arrival of the shear wave at the notch plane for Material Model (C). (a) Flow stress distribution. (b) Equivalent plastic strain rate distribution. (c) Plastic strain distribution. (d) Temperature distribution.

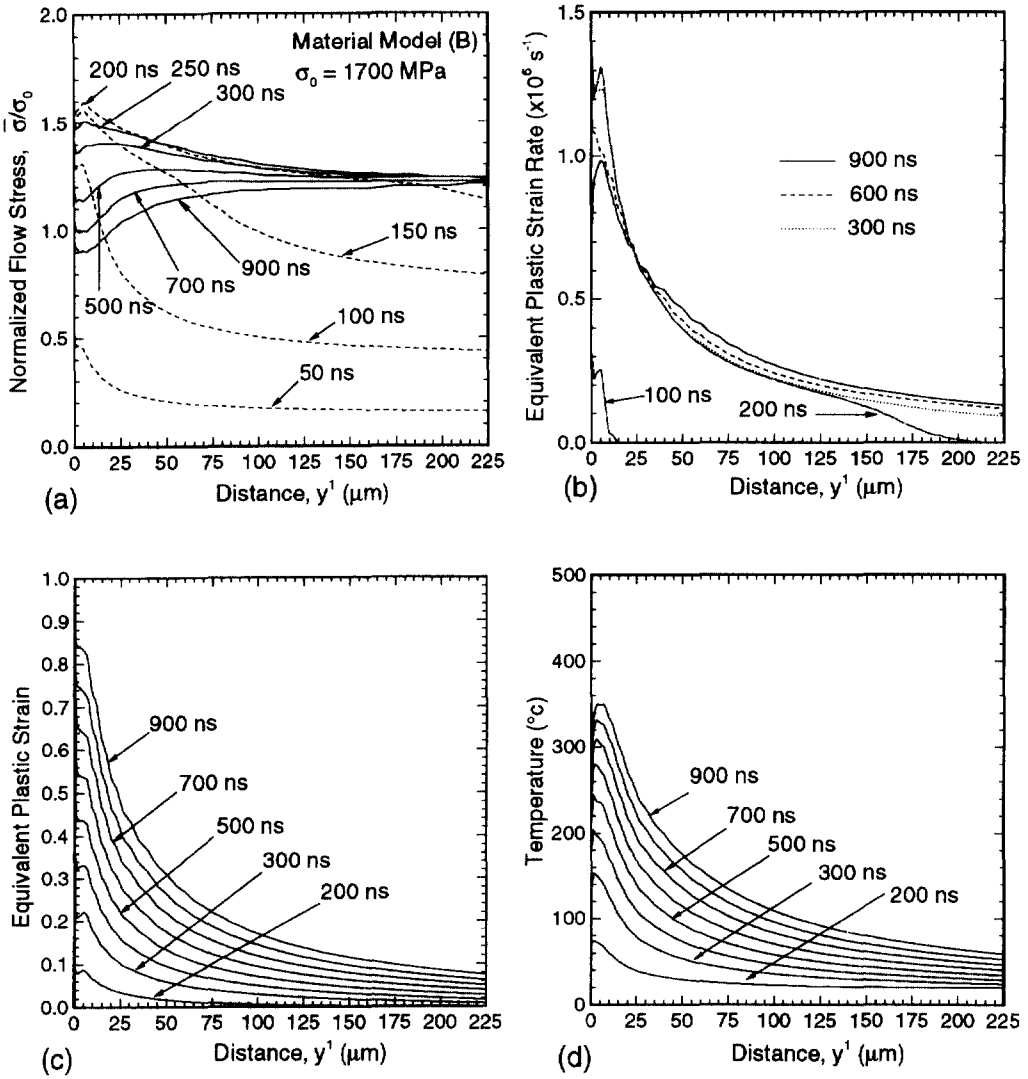

Fig. 16. Evolution of mechanical and thermal fields as a function of distance along the loading axis (y^1 axis) after the arrival of the shear wave at the notch plane for Material Model (C). (a) Normalized flow stress. (b) Equivalent plastic strain rate. (c) Equivalent plastic strain. (d) Temperature.

other hand, the propagation distance as well as the speed of propagation is reduced considerably for Material Model (A) with enhanced strain rate sensitivity. In addition, the profiles indicate that the plastic instability propagation characteristics can be divided into three distinct stages. The duration of stage I is approximately 375 ns after the arrival of the shear wave at the notch plane. During this stage the plastic instability initiates and accelerates quickly to a near constant speed of propagation. This speed of propagation is highest for Material Model (B) at 1200 m/s and is lowest for Material Model (A) (estimated to be less than 10 m/s). The speed of propagation for 4340 VAR steel is similar to that observed in Material Model (C) at 250 m/s. During Stage II, which is approximately 125 ns in duration, the speed of propagation of plastic instability decreases considerably to approximately 10 m/s for all the material models considered in the present analysis. During Stage III, the plastic instability again accelerates, but the rate of extension is considerably lower in all material models as compared to those observed in Stage I. For all cases the numerical simulations are terminated after 1000 ns of the arrival of the shear loading wave at the notch plane because of the arrival of the unloading waves at the center of the specimen from the lateral boundaries of the specimen. However, it must be noted that from Fig. 17 it is not very apparent that the shear band propagation characteristics for Material Model

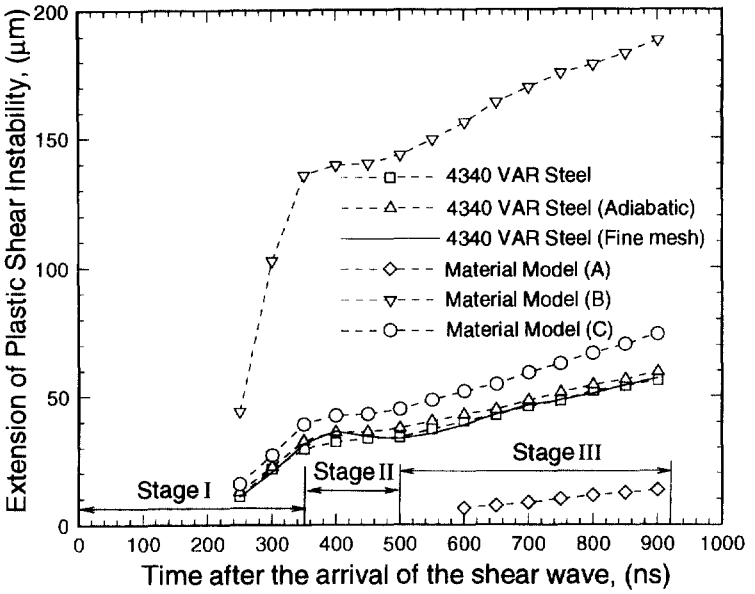

Fig. 17. Extension of plastic shear instability for 4340 VAR steel, Material Model (A), Material Model (B), Material Model (C), and Material Model (D).

(A) has three distinct stages. At present this is understood not to be a characteristic of the constitutive behavior of Material Model (A) but a consequence of the mesh employed in the present investigation. The 10×10 μm element size is unable to resolve the very small extensions of plastic instability during Stages I and II for Material Model (A), as compared to those observed in 4340 VAR steel, Material Model (B) and Material Model (C).

The solid line in Fig. 17 shows the effect of the mesh size on the aforementioned computational results. Decreasing the size of the elements while keeping the same aspect ratio in the near notch tip region leads to a slightly larger extension of the plastic instability. The finer mesh (6×6 μm), in an average sense, overestimates the extension of the shear band by approximately 8% as compared to the 10×10 μm mesh size.

4.3. *Energy partition during initiation and propagation of plastic instability*

In order to characterize material resistance to the initiation and propagation of the plastic shear instability the concept of a shear band toughness was recently proposed by Grady (1994) and reiterated by Zhou *et al.* (1996b). A realistic understanding of the issue calls for the study of the energy required for the initiation and propagation of plastic instability. To this end, the generalized path-independent J-integral for dynamic conditions is employed in the present analysis. The J-integral for dynamic loading conditions takes the form (Moran and Shih, 1987)

$$J = \int_{\Gamma} [(W+L)\,\mathrm{d}y^2 - T^i u_{i,1}\,\mathrm{d}s] + \int_A \left[\alpha \tau_k^k T_{,1} + \rho \frac{\partial^2 u^i}{\partial t^2} u_{i,1} - \rho \frac{\partial u^i}{\partial t}\left(\frac{\partial u^i}{\partial t}\right)_{,1}\right] \mathrm{d}A, \tag{62}$$

where A is the area of the contour Γ and

$$W = \int_0^{E_{ij}} \tau^{ij}\,\mathrm{d}E_{ij} - \alpha \int_0^T \tau_k^k\,\mathrm{d}T, \quad L = \frac{1}{2}\rho \frac{\partial u^i}{\partial t}\frac{\partial u_i}{\partial t}. \tag{63}$$

Since attention is focused on the initiation of the plastic instability and J-integral is path independent up to the time when a contour is intercepted by the localized band, only

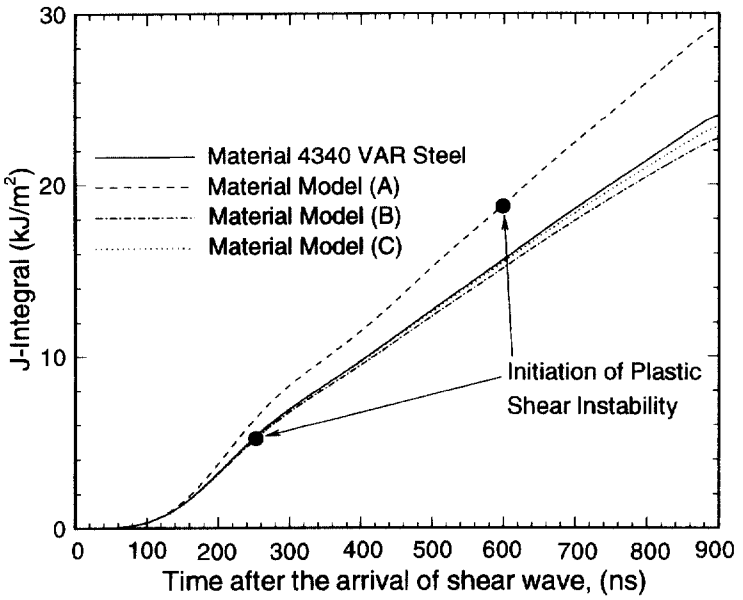

Fig. 18. Time history of J-integral for 4340 VAR steel, Material Model (A), Material Model (B), Material Model (C), and Material Model (D).

the result for the contour closest to the initial notch tip is plotted. Figure 18 shows the time histories of J-integral for the material models employed in the present study. For each material model, J-integral increases monotonically before the initiation of plastic instability occurs. It is interesting to note that the J-integral values for the initiation and propagation of plastic instability are highest for Material Model (A) for which the resistance to plastic shear deformation is the highest. Moreover, Material Model (B) posses the lowest J-integral values. This is consistent with the ease by which plastic instability initiated and propagated in Material Model (B). Also, the J-integral values for Material Model (C) lies in between the values obtained for 4340 VAR steel and Material Model (B). Again, this is consistent with the plastic instability growth characteristics observed for Material Model (C). Also it is to be noted that the J-integral values at the initiation of plastic instability, for the material models considered in the present investigation, are approximately an order of magnitude lower than those obtained for C-300 steel by Zhou *et al.* This mismatch is to be expected since, (a) the J-integral values reported by Zhou *et al.* are for the initiation of adiabatic shear banding rather than the initiation of plastic shear instability. Since, it is well understood that plastic shear instability is a precursor to adiabatic shear banding it is not surprising that the energy required for the initiation of shear banding is higher than required for just the initiation of plastic shear instability, and (b) the diameter of the pre-machined notch in the specimens used in the experiments by Zhou *et al.* is 200 μm as compared to 10 μm employed in the present investigation. The much sharper notch used in the present computations is expected to drastically lower the energy for the initiation of plastic instability.

In addition to energy absorption, energy partitioning provides another perspective on the coupled thermo-mechanical processes during the propagation of plastic instability. The work done by the imposed loading can be expressed as

$$\int_S \mathbf{f}\cdot\dot{\mathbf{u}}\,\mathrm{d}S = \frac{\mathrm{d}}{\mathrm{d}t}\int_V \frac{1}{2}\rho_0\dot{\mathbf{u}}\cdot\dot{\mathbf{u}}\,\mathrm{d}V + \int_V \boldsymbol{\tau}:\mathbf{D}\,\mathrm{d}V. \tag{64}$$

This identity specifies the balance between the rates at which mechanical work performed through the specimen boundary, the stress power and the rate of change of kinetic energy in the specimen. The stress power consists of an elastic part, a plastic part and a thermal part, i.e.

$$\int_V \boldsymbol{\tau}:\mathbf{D}\,\mathrm{d}V = \int_V \boldsymbol{\tau}:\mathbf{D}^{\mathrm{e}}\,\mathrm{d}V + \int_V \boldsymbol{\tau}:\mathbf{D}^{\mathrm{p}}\,\mathrm{d}V + \int_V \boldsymbol{\tau}:\alpha\dot{T}\mathbf{I}\,\mathrm{d}V. \tag{65}$$

Integrating (64) in time yields

$$\int_0^t \int_S \mathbf{f}\cdot\dot{\mathbf{u}}\,\mathrm{d}S = \int_V \frac{1}{2}\rho_0\dot{\mathbf{u}}\cdot\dot{\mathbf{u}}\,\mathrm{d}V + \int_0^t \int_V \boldsymbol{\tau}:\mathbf{D}\,\mathrm{d}V, \tag{66}$$

where $P(t) = \int_0^t \int_S \mathbf{f}\cdot\dot{\mathbf{u}}\,\mathrm{d}S\,\mathrm{d}t$ is the accumulated boundary work at time t, $K(t) = \int_V \frac{1}{2}\rho\dot{\mathbf{u}}\cdot\dot{\mathbf{u}}\,\mathrm{d}V$ is the total kinetic energy in the specimen and $W(t) = \int_0^t \int_V \boldsymbol{\tau}:\mathbf{D}\,\mathrm{d}V\,\mathrm{d}t$ is the accumulated stress work at time t.

Figure 19(a) and (b) show the evolution of the boundary work P, stress work W (elastic, plastic and thermal), and kinetic energy K for Material Model (A) and Material Model (B), respectively. The choice for these two materials is governed by their vastly different shear instability growth characteristics. For both cases, the boundary work P, which is the total work imparted to the specimen through the impact face increases linearly upto 1 μs, after which it remains essentially constant. The total stress work, W, and the kinetic energy, K, also increases linearly upto the time the shear wave reaches the notch plane, indicating that the energy stored in the specimen is primarily elastic since plastic work is negligible during this part of the deformation. At approximately 0.95 μs after impact, K exceeds W, signifying that a part of the boundary work translates into the kinetic energy. The changes in K and W are always of opposite sign when no additional work is imparted into the specimen through the boundary, indicating the interchange of kinetic and elastic energies in the specimen. At approximately 1.3 μs after impact, significant plastic work commences in the near notch tip region for Material Model (B). The magnitude of this plastic work is a small fraction of the elastic and kinetic energies, reflecting the relatively small size of the specimen area that undergoes plastic deformation. For Material Model (A), the plastic work remains essentially negligible throughout the duration of the loading. This observation is consistent with the very small extension of plastic instability observed for the case of Material Model (A). Also, during the deformation the thermal stress work remains essentially zero.

It is to be noted that, although energy balance plots are helpful in providing insight into the overall energy partitioning that occurs in the entire specimen during the plastic instability evolution and progression, they do not provide much insight into the local energy partitioning occurring in the region undergoing plastic shearing deformations. For example, in the present simulations, after the initiation of the plastic instability (at approximately 1.3 μs), the rate of increase of kinetic energy is positive up to 1.6 μs, after which the rate becomes negative. This decrease in kinetic energy cannot be associated with the growth characteristic of the plastic instability, and actually occurs due to the unloading waves from the lateral boundaries as well as the diffracted waves from the notch occupying a substantial area of the specimen.

Figures 20(a–d) and 21(a–d) show the local plastic dissipation contours in the process zone, at time intervals 200, 500, 700 and 900 ns after the arrival of the shear loading pulse at the notch plane. The two-dimensional nature of the propagating plastic shear instability gives rise to the gradient in plastic dissipation observed along the notch plane. As observed for Material Model (B) (Fig. 20(a)), the plastic dissipation contours extend quite a distance away from the notch tip before the initiation of the plastic instability. As the plastic instability propagates (Fig. 20(b–d)), the contours representing the plastic dissipation work translate with the plastic instability, with the maximum in plastic dissipation occurring well within the plastically localized band. Since, the location of maximum dissipation is closer to the notch tip, the gradient in plastic dissipation are much larger behind the location of maximum dissipation as compared to the gradients observed in front of it. The plastic dissipation contours for Material Model (A) are shown in Fig. 21(a–d). Unlike the plastic dissipation contours observed for Material Model (B), the contours are concentrated very close to the notch tip. This is consistent with the small growth of plastic instability in

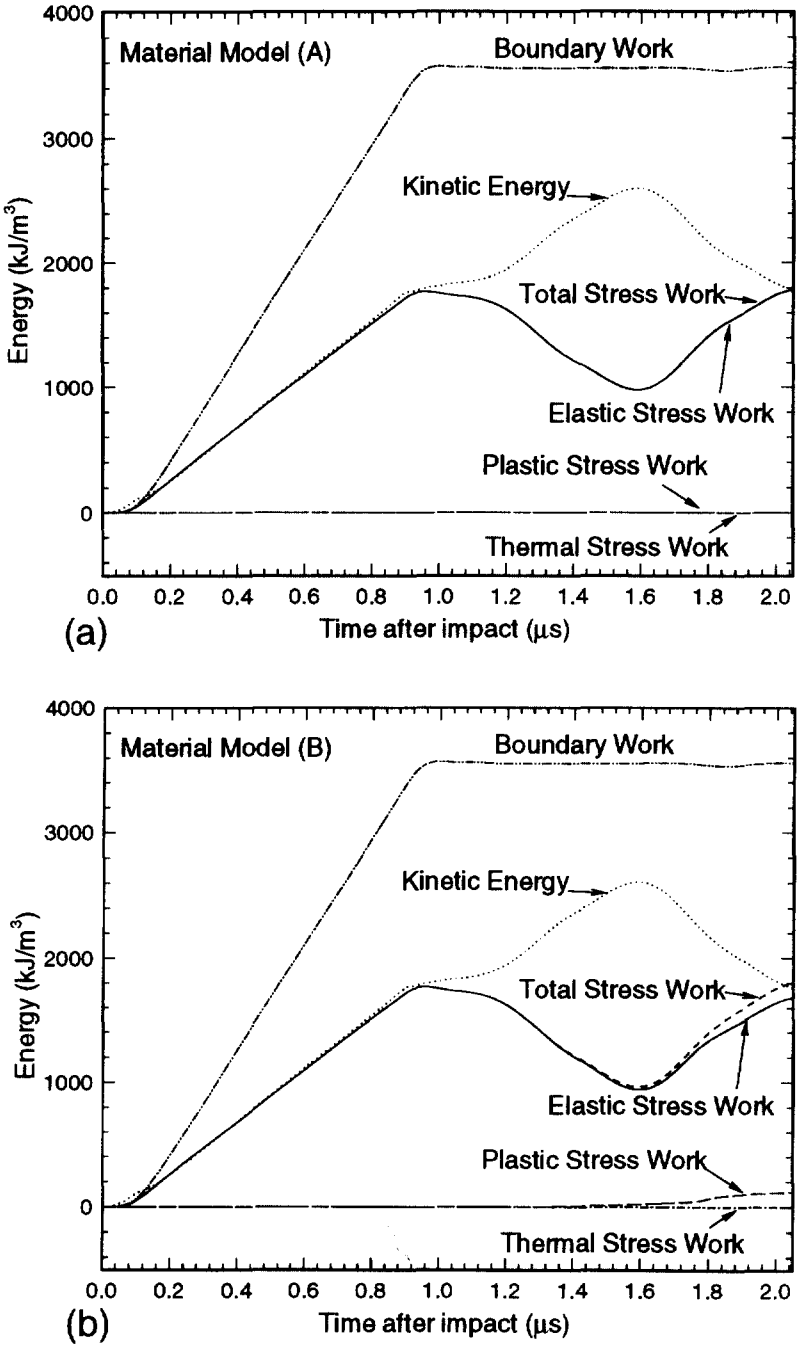

Fig. 19. Energy portioning as a function of time for, (a) Material Model (A), and (b) Material Model (B).

Material Model (A) as compared to that observed in Material Model (B). Also, as in the case of Material Model (B), the plastic dissipation contours show a maximum well within the plastic localized band. It must be noted that these observations are contrary to the assumptions employed by Grady (1992) in his analytical analysis, where the assumption of a band of zero dissipation was assumed behind the propagating shear band tip.

Acknowledgement—The computations reported in the manuscript were carried out on the Cray-YMP8 8/128 at the Ohio Supercomputer Center.

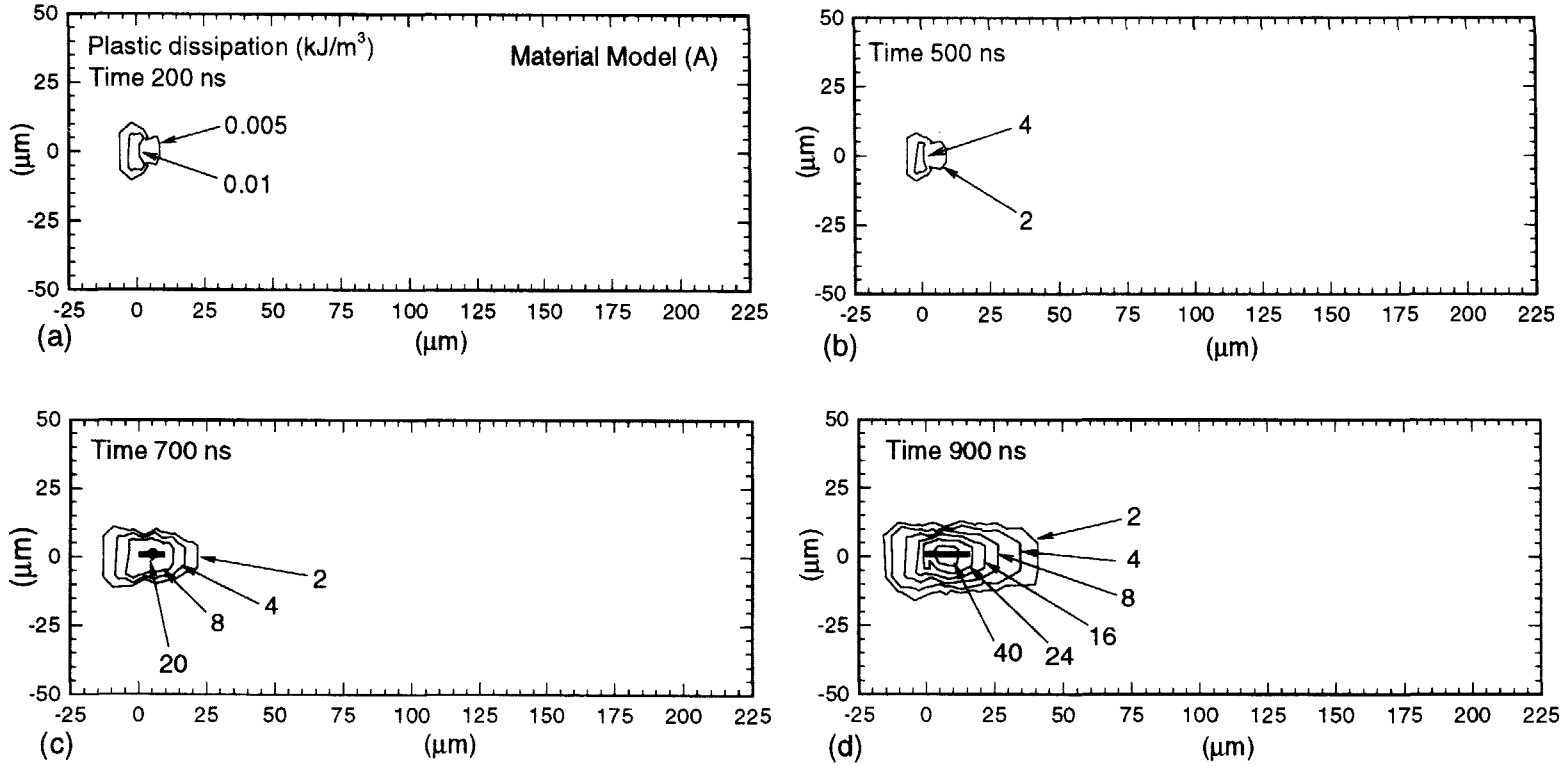

Fig. 20. Plastic dissipation due to plastic work for Material Model (B).

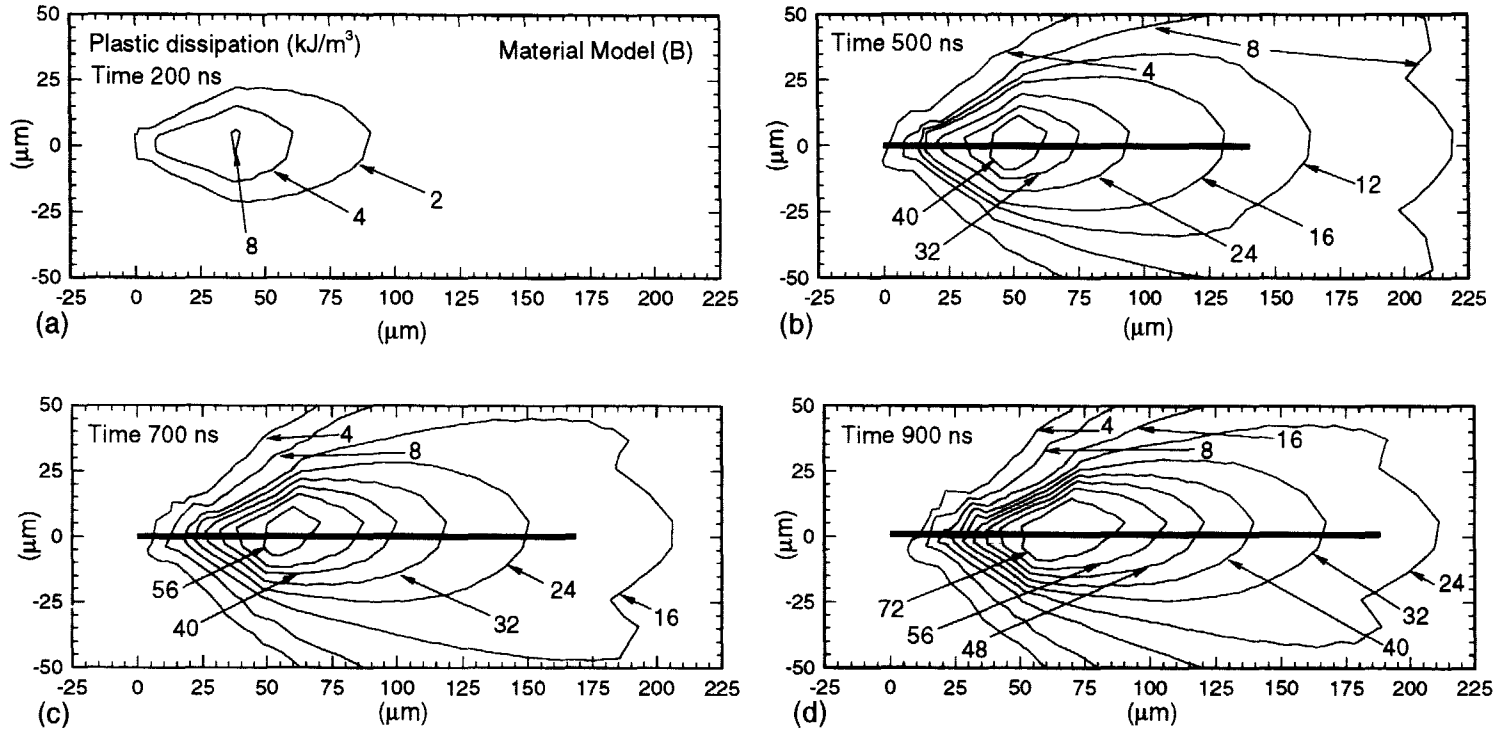

Fig. 21. Plastic dissipation due to plastic work for Material Model (A).

REFERENCES

Argon, A. S. (1973) Stability of plastic deformation. In *The Homogeneity of Plastic Deformation*, Chap. 7. ASM, Metals Park, OH.

Bai, Y. (1981) A criterion for thermo-plastic shear instability. In *Shock Wave and High Strain Rate Phenomena in Metals*, ed. M. A. Meyers and L. E. Murr, pp. 277–284. Plenum Press, New York, NY.

Bedford, A. J., Wingrove, A. L. and Thompson, K. R. L. (1974) Phenomenon of adiabatic shear deformation. *J. Aust. Inst. Metals.* **19,** 61–73.

Belytschko, T., Chiapetta, R. L. and Bartel, H. D. (1976) Efficient large scale non-linear transient analysis by finite elements. *International Journal of Numerical Methods in Engineering* **10,** 579–596.

Budiansky, B. (1969) *Remarks on Theories of Solid and Structural Mechanics: Problems of Hydrodynamics and Continuum Mechanics*, ed. M. A. Lavrent'ev *et al.*, pp. 77–83. SIAM

Canova, G. R., Kocks, U. F. and Jonas, J. J. (1984) Theory of torsion texture development. *Acta Metallica* **54,** 15–21.

Clifton, R. J. (1980) Adiabatic shear banding. In *Material Response to Ultra-High Loading Rates*, NMAB-356, Chap. 8. National Materials Advisory Board (NRC), Washington, DC.

Clifton, R. J. (1990) High strain rate behavior of metals. *Applied Mechanics Review* **43,** S10–S22.

Clifton, R. J., Duffy, J., Hartley, K. A., Shawki, T. G. (1984) On critical conditions for shear band formation at high strain rates. *Scripta Metallica* **18,** 443–448.

Culver, R. S. (1973) Thermal instability strain in dynamic plastic deformation. In *Metallurgical Effects at High Strain Rates*, ed. R. W. Rhode, B. M. Butcher, J. R. Holland and C. H. Karnes. TMS-AIME, pp. 519–528. Plenum Press, New York, NY.

Dafalias, Y. F. (1985) The plastic spin. *Journal of Applied Mechanics* **52,** 865–871.

Duffy, J. and Chi, Y. C. (1992) On the measurement of local strain and temperature during the formation of adiabatic shear bands. *Materials Science Engineering* **A157,** 195–210.

Grady, D. E. (1992) Properties of an adiabatic shear-band process zone. *Journal of the Mechanics and Physics of Solids* **40,** 1197–1215.

Grady, D. E. (1994) Dissipation in adiabatic shear bands. *Mech. and Mater.* **17,** 289–293.

Hutchinson, J. W. (1984) Introduction of the viewpoint set on shear bands. *Scripta Metallica* **18,** 421–422.

Kalthoff, J. K. and Winkler, S. (1987) Failure mode transition at high rates of shear loading. In *International Conference on Impact Loading and Dynamic Behavior of Material*, ed. C. Y. Chiem, H. D. Kunze and L. W. Meyer, **1,** 185–195.

Krieg, R. D. and Key, S. W. (1973) Transient shell response by numerical time integration. *International Journal of Numerical Methods in Engineering* **7,** 273–286.

Kuriyama, S. and Meyers, M. A. (1986) Numerical modeling of the propagation of an adiabatic shear band. *Metall. Trans.* **17A,** 443–450.

Lee, E. H. (1969) Elastic–plastic deformation at finite strains. *Journal of Applied Mechanics* **36,** 1–6.

Lee, Y. and Prakash, Y. (1995) Dynamic fracture toughness of AISI 4340 VAR steel under conditions of plane strain. *Metall. and Mater. Trans.* **26A,** 2527–2343.

Marchand, A. and Duffy, J. (1988) An experimental study of the formation process of adiabatic shear bands in a structural steel. *Journal of the Mechanics and Physics of Solids* **36,** 251–283.

Mason, J. J., Rosakis, A. J. and Ravichandran, G. (1994) Full field measurements of the dynamic deformation field around a growing adiabatic shear band at the tip of dynamically loaded crack or notch. *Journal of the Mechanics and Physics of Solids* **42,** 1679–1697.

Merzer, A. M. (1982) Modeling of adiabatic shear band development from small imperfections. *Journal of the Mechanics and Physics of Solids* **30,** 323–338.

Meyers, M. A. (1994) *Dynamic Behavior of Materials*. John Wiley and Sons, New York, NY.

Moran, J. and Shih, C. H. (1987) General treatment of crack tip contour integrals. *International Journal of Fracture* **35,** 295–310.

Nategaal, J. C., Parks, D. M. and Rice, J. R. (1974) On numerically accurate finite element solutions in the fully plastic range. *Comp. Meth. Appl. Mech. Engng* **4,** 153–175.

Needleman, A. (1985) On finite element formulations for large elastic–plastic deformations. *Composite Structures* **20,** 247–257.

Needleman, A. (1989) Dynamic shear band development in plane strain. *Journal of Applied Mechanics* **56,** 1–9.

Nemat-Nasser, S. (1992) Phenomenological theories of elastoplasticity and strain localization at high strain rates. *Applied Mechanics Review* **45**(2), S19–S45.

Olson, G. B., Mescall, J. F. and Azrin, M. (1981) Adiabatic deformation and strain localization. In *Shock Wave and High Strain Rate Phenomena in Metals*, ed. M. A. Meyers and L. E. Murr, pp. 221–247. Plenum Press, New York, NY.

Peirce, D., Shih, C. F. and Needleman, A. (1984) A tangent modulus method for rate dependent solids. *Composite Structures* **18,** 875–887.

Povirk, G. L., Needleman, A. and Nutt, S. R. (1990) An analysis of residual stress formulation in whisker-reinforced Al–SiC composites. *Mater. Sci. and Engng* **A125,** 129–140.

Prakash, V. and Clifton, R. J. (1992) Experimental and analytical investigation of dynamic fracture under condition of plane strain. *ASTM STP* 1, ed. H. A. Ernst, A. Saxena and D. L. Dowell, pp. 412–444. ASTM, Philadelphia, PA.

Ravichandran, G. and Clifton, R. J. (1989) Dynamic fracture under plane wave loading. *International Journal of Fracture* **40,** 157–201.

Ravi-Chandar, K. (1995) On the failure mode transition in polycarbonate under dynamic mixed-mode loading. *International Journal of Solids and Structures* **32,** 925–937.

Recht, R. F. (1964) Catastrophic thermoplastic shear. *Journal of Applied Mechanics* **31,** 189–196.

Rogers, H. C. (1979) Adiabatic plastic deformation. *Ann. Rev. Mater. Sci.* **9,** 283–311.

Rogers, H. C. (1983) Adiabatic shearing—general nature and material aspects. In *Material Behavior Under High Stress and Ultra-high Loading Rates*, ed. J. Mescall and V. Weiss, pp. 101–112. Plenum Press, New York, NY.

Seimiatin, S. L., Staker, M. R. and Jonas, J. J. (1984) Plastic instability and flow localization in shear at high rates of deformation. *Acta Metallica* **32,** 1347–1354.

Taylor, G. I. and Quinney, H. (1934) The latent energy remaining in a metal after cold working. *Proceedings of the Royal Society of London* **A143,** 307–326.

Timothy, S. P. (1987) The structure of adiabatic shear bands in metals: a critical review. *Acta Metallica* **35,** 301–306.

Tvergaard, V. (1981) Influence of voids on shear band instabilities under plane strain conditions. *International Journal of Fracture* **17,** 389–407.

Tvergaard, V., Needleman, A. and Lo, K. K. (1981) Flow localization in the plane strain tensile test. *Journal of the Mechanics and Physics of Solids* **29,** 115–142.

Wright, T. W. and Walter, J. W. (1987) On stress collapse in an adiabatic shear band. *Journal of the Mechanics and Physics of Solids* **35,** 701–720.

Wright, T. W. and Walter, J. W. (1996) The asymptotic structure of an adiabatic shear band in anti-plane motion. *Journal of the Mechanics and Physics of Solids* **44,** 77–97.

Zhou, M., Ravichandran, G. and Rosakis, A. J. (1996a) Dynamicaly propagating shear bands in impact-loaded pre-notched plates, I—experimental investigation of temperature signatures and propagation speed. *Journal of the Mechanics and Physics of Solids* **44,** 981–1006.

Zhou, M., Ravichandran, G. and Rosakis, A. J. (1996b) Dynamically propagating shear bands in impact-loaded pre-notched plates, II—numerical simulation. *Journal of the Mechanics and Physics of Solids* **44,** 1007–1032.

Zurek, A. K. (1994) The study of adiabatic shear band instability in a pearlitic 4340 steel using a dynamic punch test. *Metall. and Mater. Trans.* **25A,** 2483–2489.